ALMA MATER STUDIORUM- UNIVERSITA' DI BOLOGNA
CAMPUS DI CESENA

SCUOLA DI INGEGNERIA E ARCHITETTURA

CORSO DI LAUREA MAGISTRALE IN INGEGNERIA BIOMEDICA

MULTIPLE PATHOGEN DETECTION USING NANOPLASMONIC SENSING

Tesi in

Biochimica

Relatore:

Emanuele Domenico Giordano

Presentata da:

Chiara Filippini

Sessione: I° sessione

Anno Accademico: 2013/2014

ABSTRACT

Opportunistic diseases caused by Human Immunodeficiency Virus (HIV) and Hepatitis B Virus (HBV) is an omnipresent global challenge. In order to manage these epidemics, we need to have low cost and easily deployable platforms at the point-of-care in high congestions regions like airports and public transit systems. In this dissertation we present our findings in using Localized Surface Plasmon Resonance (LSPR)-based detection of pathogens and other clinically relevant applications using microfluidic platforms at the point-of-care setting in resource constrained environment. The work presented here adopts the novel technique of LSPR to multiplex a lab-on-a-chip device capable of quantitatively detecting various types of intact viruses and its various subtypes, based on the principle of a change in wavelength occurring when metal nano-particle surface is modified with a specific surface chemistry allowing the binding of a desired pathogen to a specific antibody. We demonstrate the ability to detect and quantify subtype A, B, C, D, E, G and panel HIV with a specificity of down to 100 copies/mL using both whole blood sample and HIV-patient blood sample discarded from clinics. These results were compared against the gold standard Reverse Transcriptase Polymerase Chain Reaction (RT-qPCR). This microfluidic device has a total evaluation time for the assays of about 70 minutes, where 60 minutes is needed for the capture and 10 minutes for data acquisition and processing. This LOC platform

eliminates the need for any sample preparation before processing. This platform is highly multiplexable as the same surface chemistry can be adapted to capture and detect several other pathogens like dengue virus, E. coli, M. Tuberculosis, etc.

Keywords: HIV * Point-of-care * LSPR * lab-on-a-chip * RT-qPCR * *E. coli* * HBV

Table of Contents

Chapter 1

Review of point-of-care diagnostic technologies

1.1 Introduction

In the past two decades, the role-played by nanotechnology and Micro-technology has been crucial for the growth of the research in fields like biomedical engineering and chemical engineering. These technologies are now emerging as important tools that can be used even in resource constrained settings and in many developing countries that lack the basic infrastructure to support large scale clinical diagnostic laboratories. Instead we are now moving into an era where we are bringing the entire lab at the point-of-care so that patients who are not able to access such expensive diagnostic tool can have early stage detection of diseases caused by pathogens. The work done by Won G. Lee et al. [1] at the Bio-Acoustics MEMS in Medicine Laboratory and Center for Biomedical Engineering at the Brigham and Women's Hospital, brings to light some very important developments in the field of microfluidics that can aid in the detection of diseases in resource constrained setting.

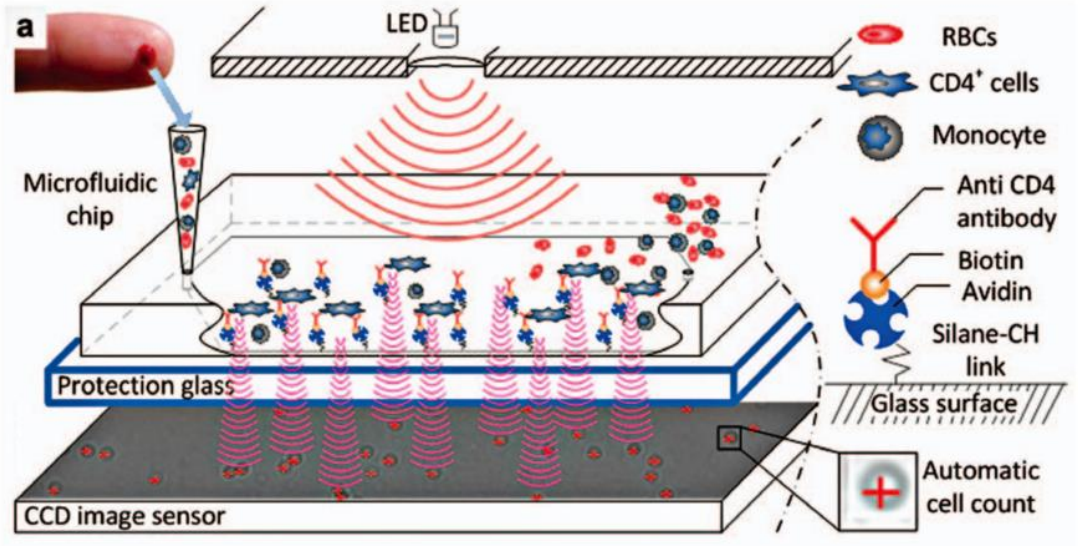

Figure 1: The use of finger prick amount of blood to perform rapid test at the POC. Ref [1]

These micro scale platforms offer immense possibilities like manipulation of fluids in channels of sub-millimeter scale, which is a very important step in many assay processing for pathogen detection. Reports published by the United States Center for Disease Control states that nearly 94.8% deaths in many developing countries is primarily due to the lack of timely diagnosis or affordable healthcare.

In response to the increasing need for early detection of pathogens, the World Health Organization has set up the ASSURED protocol, which calls for new technologies to be: "**A**ffordable, **S**pecific, **S**ensitive, **U**ser-friendly, **R**obust, **E**quipment free and **D**elivery to the needy" [1]. Based on these guidelines many researchers are now developing point-of-care devices that help in reducing costs and improving detection capabilities of microchip [12].

One of the important features of microfluidics is the fabrication that has been adapted from VLSI technology and evolved to suit plastic based fabrication. The need for high capillarity surface calls for materials engineering and the use of materials like PMMA, PDMS, DSA, FLASH, etc. all of which respond well to lithography and laser cutting based design and fabrication.

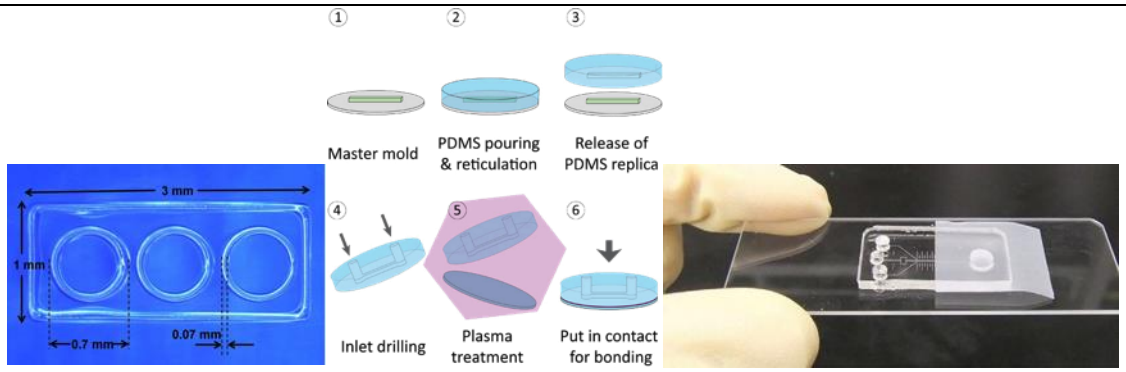

Figure 2: Materials like PMMA, PDMS and Glass chips. Ref.[2]

1.2 Categories of Research development

Broadly we can categorize the various developments in the field of microfluidics as follows, each of which has been described in the following section.

1. **Microchip imaging and detection:** Imaging and detection based on microfluidic chips can be achieved using several methods. The most important of which are: Optical microscopy, opto-fluidics (the fusion of imaging and microfluidics), and detection using methods like SPR, LSPR, absorbance, fluorescence, interferometer, or luminescence. Other methods include the use of Portable CCD, and more recent technologies like mobile phone based imaging and microscopy [12].

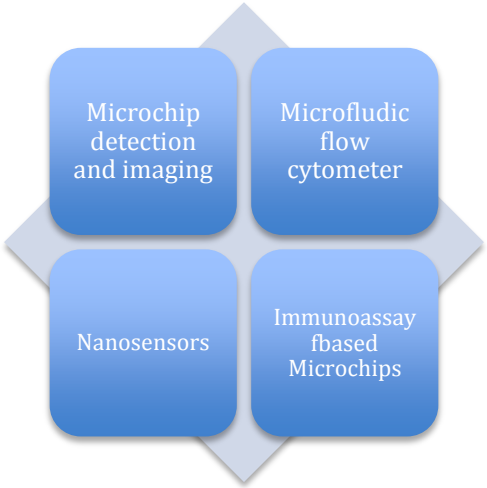

Figure 2a: Various categories of development in Micro/Nanotechnology

2. **Flow cytometer microfluidics:** The most important feature of microfluidic flow cytometer are: label-free detection, lens less imaging, simple design of channels, sheath-free focusing [9].
3. **Immunoassay based chips:** Recent developments in the area of immunoassay include a miniature ELISA chips to perform Rapid Diagnostic Test (RDT), other devices include those based on lateral flow and diffusion. Microchips with diffusion based immunoassay for detecting quantities of small molecules have also been developed.
4. **Nanosensors:** There are many new nano-devices that are capable of detecting extremely low amounts of nanoparticles like DNA and viruses. Some notable devices

are: nanotubes and nanowires based on CNT, AFM based detection, glass- based ViriChip, etc. [9,12].

The integration of all these types of sensors into one global healthcare network is the general direction of research in health science and information technology. Achieving such level of comprehensive network integration [9] would mean that virtually patient and healthcare provider can be separated geographically and yet interact with concrete clinical data at the patient end.

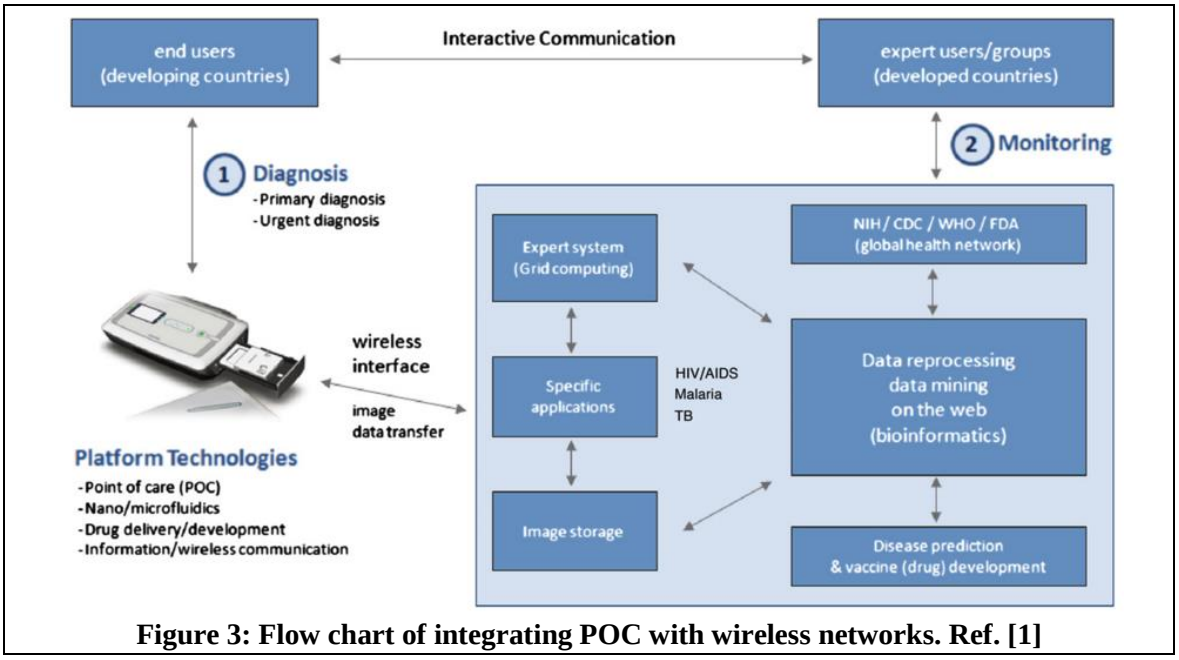

Figure 3: Flow chart of integrating POC with wireless networks. Ref. [1]

The CCD works on the principle, where the shadow of the image of the cells falls on the photoactive surface of the CCD [9,12] and this change in intensity produces electrical charge that is imaged and tracked. In order to illustrate the devices like CCD and DAPI staining we illustrate the following:

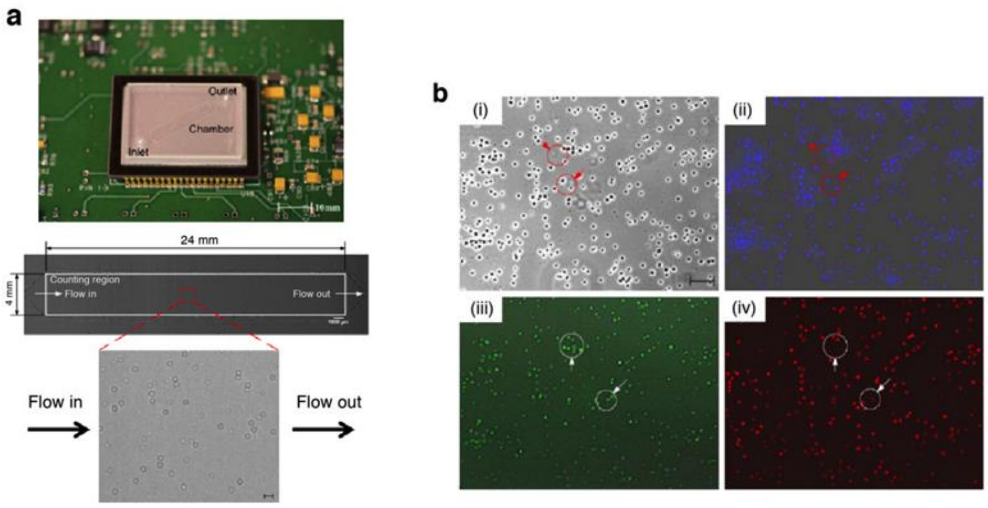

Figure 4 a. CCD Imaging of chips with flow of CD 4 T lymphocyte cells, 4b. Phase contrast, DAPI imaging, CD4+ stain, CD3+ stain cells. Ref.[1]

The rapid growth of these micro technologies makes it possible to detect diseases like Malaria using the lateral flow based immunoassay sensors. Lateral flow based Rapid Detection Tests (RDT) are very commonly used for Malaria diagnosis. A few decades microscopy of the blood sample was considered the "gold-standard" of detection. These RDT based chips are able to sense the proteins in the blood of Malaria patients. The chip if tested positive would display a series of lines to show the binding of antigen with antibody at the lines. It must be noted that such chips must have channels that are able to accommodate the cells found in the blood, ranging from RBC to WBC [9]. This device has been illustrated below in Figure 5.

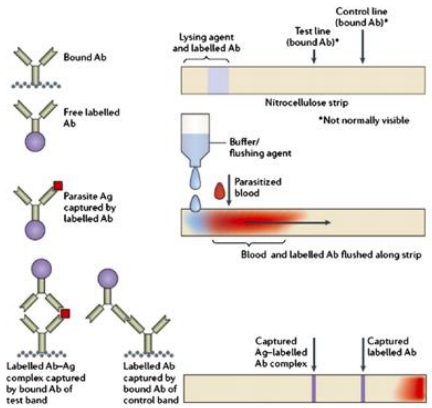

Figure 5: RDT chip for the detection of Malaria. Ref [9]

It has also been estimated that nearly a third of the world's population has been affected with Latent form of Tuberculosis infection or have actually contracted the disease in its active form. In order to detect TB at an early stage T. Spot test is done along with the Tuberculin Skin Test (TST). However, those who are asymptomatic may not be diagnosed at all until they actually develop the TB infection [9,12]. The study done by H. Lee et al. on the use of magnetic nanoparticles based NMR method of detecting TB has shown promising results for use in resource constrained setting. When the magnetic NP (MNP) are in monodispense state of about 38 nm in size, the relaxation time of the NMR is linearly decreasing with T= 40 ms. However when the MNP form clusters and size increases to 300 nm, the magnetic relaxation time fall faster at T= 14 ms. An integrated micro RF coil on a chip can be used to excite the system and produce the required magnetic excitation.

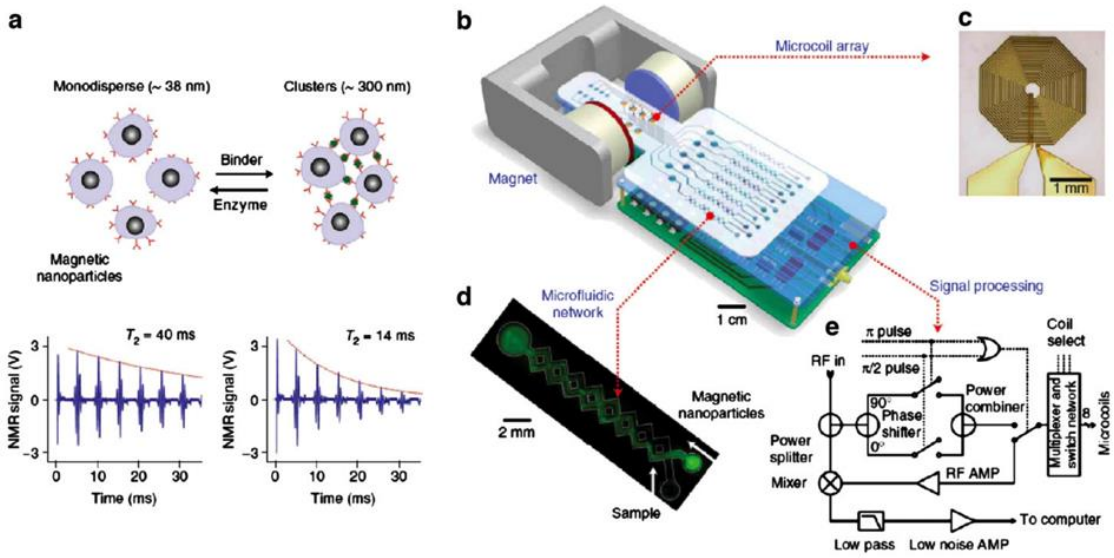

Figure 6: TB detection chip using NMR a. Assay containing MNP, b. Device schematic, c. RF micro coil to excite the MNP in the assay, d. The microfluidic network channel, e. The signal processing circuit. Ref [9]

We have also seen the increasing trend in Cell Phone based microscopy and imaging that has helped in connecting patients from remote locations with the primary care provider. Portable CCD are also an effective alternative to provide reliable results in case of blood samples with border limit amounts of biomarkers. In conclusion to Chapter 1, we see the increasing trend in the use of POC device at resource-constrained settings for monitoring the spread of diseases and pathogens. From HIV/AIDS, to Tuberculosis on a chip and Malaria detection using RDT immunoassay based chips, LOC devices are being adapted to meet the pathological needs of various disease detection gold standard protocols [12].

Chapter 2

Physics of Localized Surface Plasmon Resonance

2.1 Introduction

Surface Plasmon resonance (SPR) and localized surface plasmon resonance (LSPR) are both powerful tools for label-free bio-sensing in biochemistry due to their high sensitivity to the refractive index change caused by their interactions with molecules such as DNA or proteins, etc. SPR is known as a phenomenon excited when the frequency of evanescent electromagnetic wave propagating at the metal-dielectric interface is resonant with the oscillation of the surface conduction electrons in metal [40]. LSPR often refers to metallic nanoparticles as it occurs when the frequency of incident photon is resonant with the collective oscillation of conduction electrons in metallic nanoparticles. Bio-sensing has traditionally employed spectroscopic techniques that measure biological interactions in solution; however, performing assays on a surface has certain advantages: surface assays require less sample than solution assays; they permit real-time measurements; they are readily amenable to high throughput sensing since probe functionalized surfaces are easily washed and regenerated enabling sequential measurements; and a single surface can be functionalized with an assortment of probes for multiplexed simultaneous sensing [41]. SPR and LSPR technologies are based on the wave propagation or electromagnetic field enhancement phenomena near metal surfaces or nanoparticles. The propagating surface plasmon polaritons excited on plane metal surfaces are utilized in SPR sensors. LSPR relies on the field enhancement and confinement in close proximity to nanoparticles. The localized field oscillations around nanoparticles motivate the name “localized” in LSPR. The plasmon modes extend up to a few tens of nanometers in LSPR sensors, allowing sensitive sub-wavelength biosensors. SPR biosensors interrogate the resonance angle changes to detect and quantify bioagents. LSPR measurements are in the form of absorbance or spectral shift data obtained from extinction curves. In general, sensitivities of these resonance or extinction shifts to refractive index changes are used to quantify figure of merit parameters for SPR and LSPR sensors[42].

2.2 Physics principles

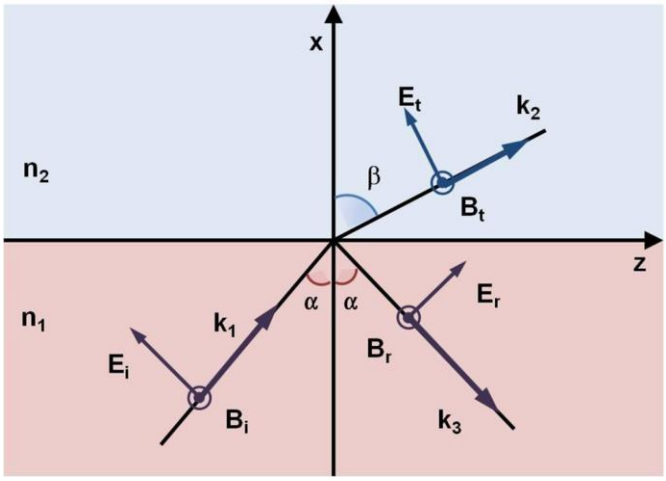

Figure 7: Plane-wave, refracting, and reflecting light at a metal−dielectric interface. n2 and n1 are the refractive indices of the metal and the dielectric mediums. E is the electric field vector, B is the magnetic field vector, and k is the wavevector. The indices i, r, and t are for incident, reflecting and refracting light. The magnetic field is perpendicular to the plane of incidence, representing transverse magnetic light.

To analyze the propagation of surface plasmons along a metal−dielectric boundary, we consider the reflection and refraction of light between two infinite media. A linearly polarized, monochromatic light propagates from the dielectric medium toward the metallic surface, as shown in Figure **7** [41]. To explain the SPR theory, transverse magnetic (TM) polarized incident light is used. TM polarization indicates that the magnetic field vector is in the plane of the metal−dielectric interface. There is no loss of generality in using TM polarization, since transverse electric modes cannot excite surface plasmons. Solving Maxwell's equations for the p-polarized light for the wavevector components, one can find the surface plasmon dispersion relation**:**

$$K_{1z} = \frac{\omega}{c}\sqrt{\frac{\varepsilon_1\varepsilon_2}{\varepsilon_1+\varepsilon_2}} \qquad K_{1x} = \frac{\omega}{c}\sqrt{\frac{\varepsilon_1^2}{\varepsilon_1+\varepsilon_2}}$$

Here, the medium is indicated by the first subscript (i.e., i = 1 for dielectric medium and i= 2 for metal medium), the axis is indicated by the second subscript, k is the wavevector,

ω is the angular frequency of the light, c is the speed of light in vacuum, n_2 and n_1 are the refractive indices for the metal and the dielectric media, respectively, $\varepsilon_1 = n_1^2$, $\varepsilon_2 = n_2^2$, and ε_1 and ε_2 are the dielectric constants of the media. From the boundary conditions it also follows that k1z = k2z. Since medium 2 is a metal, the dielectric constant ε_2 and K_{1x} are complex-valued quantities, resulting in the exponential decay of the plasmon field in both media, in the direction of the x-axis. This decay results in a surface wave, confined to the metal−dielectric interface [40]. Physically, the incident photons couple to the free electrons on the interface, resulting in a propagating surface charge-density oscillation. The K_{1z} component of the wavevector defines the wavelength of the resonance oscillation and also the extent of the plasmon wave over the interface before absorption by the metal. For long-range and bound plasmon waves in an ideal, lossless medium, a real-valued K_{1z} and an imaginary-valued K_{1x} are required, i.e. ε1*ε2 < 0 and ε1 + ε2 < 0, ignoring the imaginary parts of the dielectric constants. At optical wavelengths these two conditions are satisfied for gold and silver, which are commonly used metals in SPR experiments. Field components of the plasmon modes take their highest values at the interface and exponentially decay into the metal and dielectric media. The penetration depth of the fields into both mediums are given by 1/Im(K_{1x}) and 1/Im (K_{2x}), where Im is the imaginary part. The penetration depth in the dielectric media is on the order of half the wavelength of the incident light. For instance, for a gold−water interface and λ = 700 nm, the penetration depth in water can be calculated to be around 238 nm. When there is a local change in the dielectric constant over the metal layer, which is caused by a molecular binding event, the surface plasmon mode energy will be changed [2]. The SPR biosensors rely on this property of the resonance. Since the total energy of the system is conserved, the change in the plasmon mode's energy will leave a signature on the reflected or transmitted light. In SPR biosensor applications, light is monitored and analyzed to extract binding and kinetic information. This analysis is related to which method is utilized to couple the light to plasmon modes.

2.2.1 Physical absorption

Physical adsorption technique utilizes the surface characteristics and surface charge to attach and immobilize biorecognition elements onto the surface and relies on nonspecific physical interactions between the recognition element and the support material. In contrast to chemical binding techniques, this method also holds a key advantage since it does not require any reagent to activate chemical groups on the surface, and thus, this technique is easy to perform, inexpensive, and reduces structural damage in biorecognition elements. The physical adsorption method particularly utilizes hydrogen bonding and van der Waals forces. These weak interactions also allow the biorecognition elements to easily detach from the surface, and thus, the biosensing surface can be used multiple times [30]. However, nonspecific physical interactions are closely affected by environmental changes, including temperature, ionic content, and pH. On the other hand, this technique causes nonspecific binding of other molecules and substances, resulting in a significant decrease in surface coverage of the recognition elements and sensor specificity. The support materials can be modified to generate surface charge and reactive groups using oxidizing techniques such as oxygen plasma treatment. On plasma-treated slides, the binding amount of oligonucleotide−protein conjugates significantly increased compared to untreated slides. Another interesting observation in this study was that plasma treatment amplified the surface area and formed nanoroughened structures that could facilitate detection of a low amount of target analyte and improve the analytical performance of the biosensing surface in microarray applications. Although oxygen plasma treatment is a simple and effective method for many surfaces, it often causes significant damage on the biosensing support surface [31]. This major obstacle leads to permanent surface disruptions, which interfere with the sensor surface structure and reduce sensitivity. On the other hand, the surface characteristics (e.g., hydrophobicity and polarity) and the functional groups of biomolecules determine the molecular interactions for biomolecule immobilization. Although, in some cases, the orientation of the recognition element is not critical to capture the target analyte, these molecular changes on the surface can affect biomolecular activity (e.g., denaturation of proteins) and orientation of proteins and antibodies due to the restrictions in their conformational flexibility.

2.2.2 Principle of detection:

The entire principle of detection for the pathogens and other biological entities like live cells from the human body or drugs that are being multiplexed on the microfluidic platform rely on the physics of Localized Surface Plasmon Resonance. As depicted in Figure 8 below, we can see than a single frequency (monotone) light is shone on the sample at a particular angle of incidence. A prism placed in the near field split the monotone light such that multiple rays of light shine at various angles of incidence. When the electromagnetic wave hit the surface containing some type of surface chemistry over the Gold nanoparticle layer, the metal NP absorb some amount of energy and produce Surface Plasmon Polaritons (SPP). These waves propagate [17] along the surface and are called Plasmon waves. The remaining incident light is reflected off the surface or transmitted (depending on the optical set up) with a frequency spectrum component that is different from that of the incident radiation.

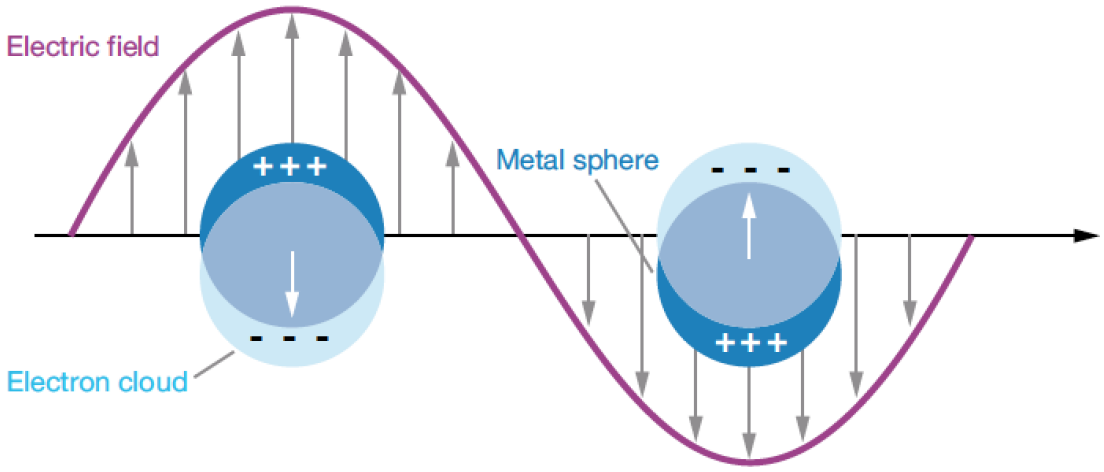

Figure 8: Physics of Surface Plasmon Resonance. Ref [17]

From the spectrum band we can detect the range of frequencies that were absorbed by the microfluidic platform by virtue of the surface modified layers over the metal NP. In order to illustrate the effect of surface modification on the spectrum of absorbance, we show in Figure 8a the surface containing conjugated antigen and antibody.

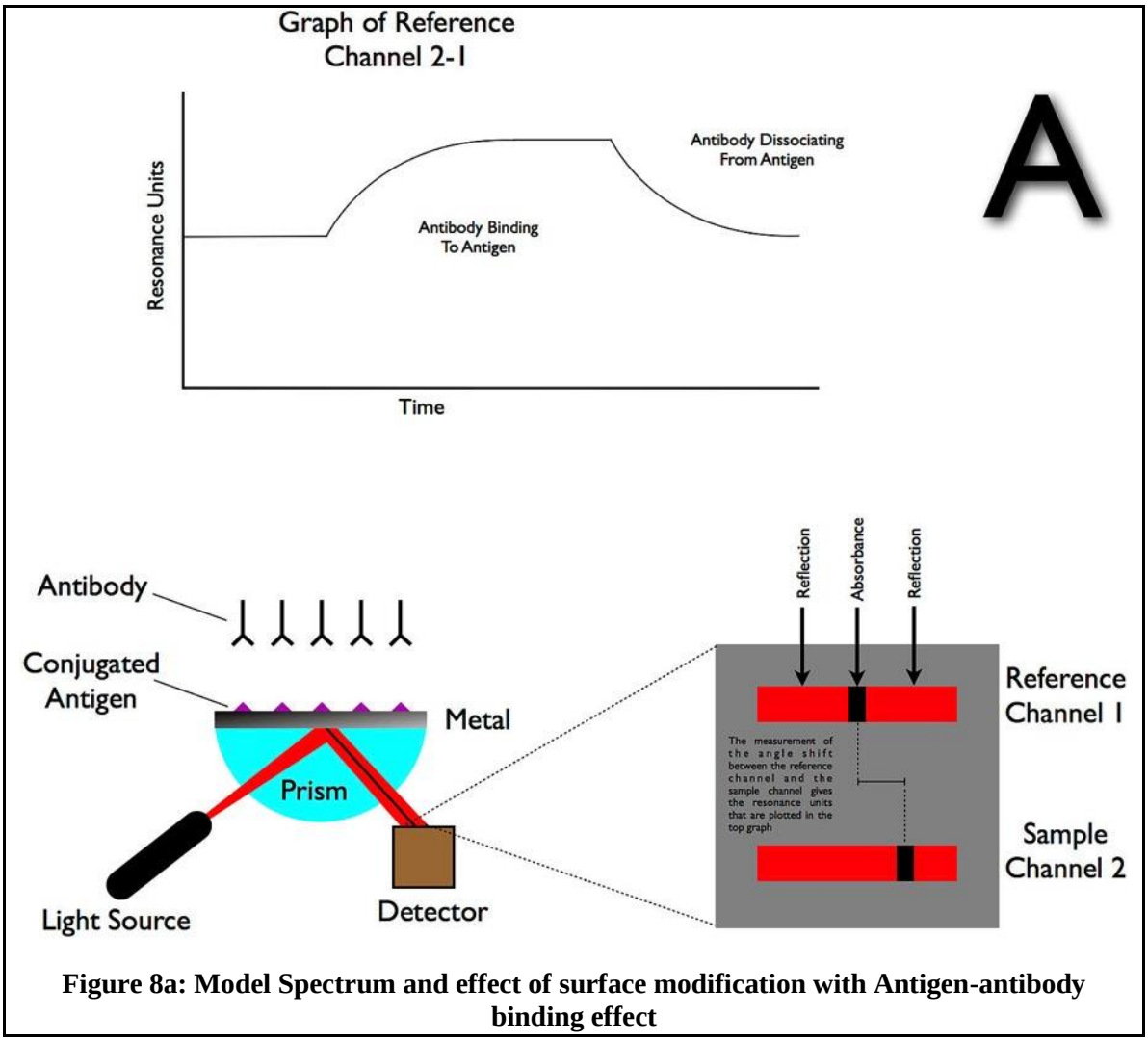

Figure 8a: Model Spectrum and effect of surface modification with Antigen-antibody binding effect

From the above graph we can see that before adding any receptor that frequency spectrum has a specific band of absorbance. However when there is also a receptor along with the antigen antibody, the spectrum is different from the previous one obtained. As shown in Figure 8b the resonance plot has two different regions. In the first region the association and dissociation effect of the antibody [1,2,3] is shown and the second curve shows the effect of receptor binding on the spectrum.

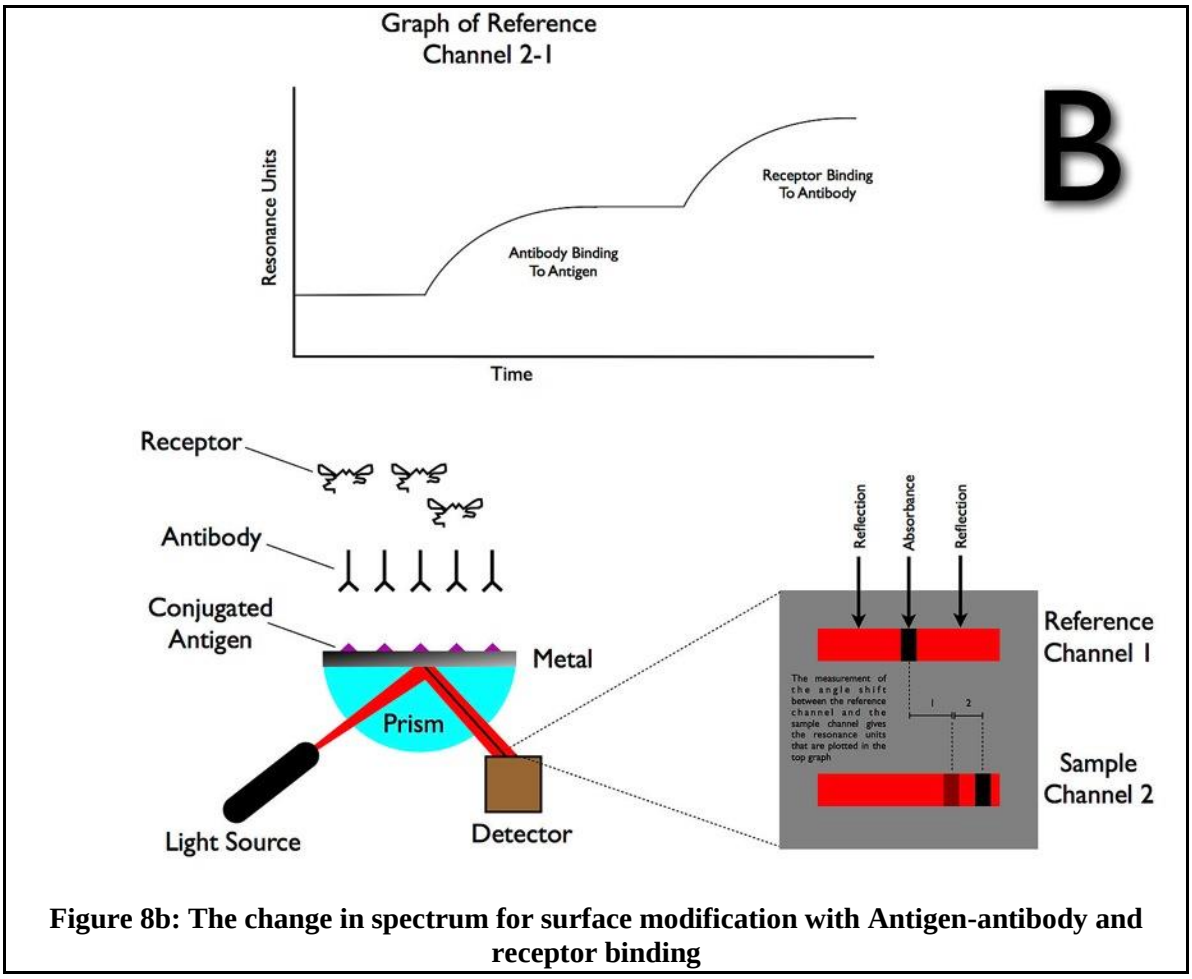

Figure 8b: The change in spectrum for surface modification with Antigen-antibody and receptor binding

2.3 Characteristics of LSPR and SPR.

The terminology "resonance" is used to highlight the match in frequency between the incident electromagnetic radiation and the frequency of the generated surface plasmon electrons waves (these electrons vibrate to and fro by virtue of the nuclear attraction in a polarized atom). This technique of LSPR [1,3,17] is very sensitive to any surface modification as this surface forms the boundary interface where SPP is generated. The materials dielectric constant at the interface changes in response to any addition biological species or chemical molecules. The addition of such molecules gives rise to a complex electrical permittivity to the metal NP, which causes absorption of the incident radiation. The SPP produced have higher amplitudes of oscillation in the near field resonant condition. Another important characteristic of the SPP waves is that, they have

maximum intensity in the metal NP and decay rapidly outside the NP-dielectric interface. In order to generate SPP waves, the incoming electromagnetic radiation needs to be p-polarized, which means the waves in parallel polarized to the incident plane. If the incoming radiation has a polarization perpendicular to the surface, such a wave would be incapable to generating SPP. The generated SPP obey the below relation, known as the dispersion equation:

$$K(\omega) = \frac{\omega}{c}\sqrt{\frac{\varepsilon 1 \mu 1 \varepsilon 2 \mu 2}{\varepsilon 1 \mu 1 + \varepsilon 2 \mu 2}}$$

where, $\varepsilon 1$ is the electrical permittivity and $\mu 1$ is the magnetic permeability of the interface. The Varioskan scanning machine uses a Kretschmann configuration [17] of generating SPP, in which the prism is placed in close proximity to the surface. This configuration is also one of the most commonly used in commercial devices, as opposed to the Otto Configuration of prism arrangement, which relies on the evanescent radiation to excite SPP.

The other important advantage of LSPR based microfluidic detection platform is the label free nature of detection. In conventional methods like Enzyme Linked Immunosorbent Assay (ELISA) or Lateral Flow Assay (LFA), the detection is dependent on a secondary label and multiple processing steps involving rinsing [1,3].

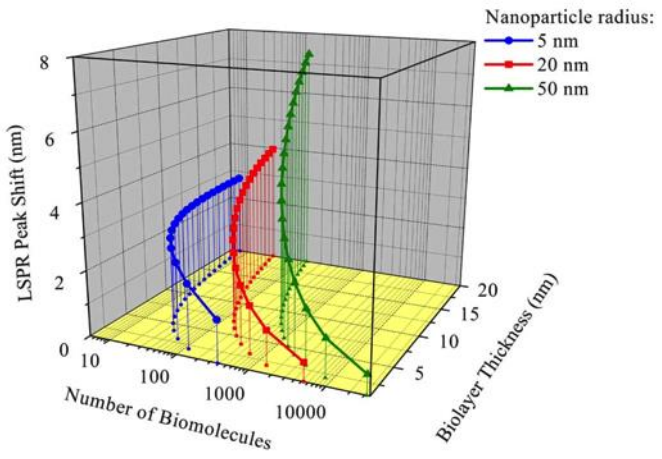

Figure 9: Relation between LSPR Peak shift and Number of biomolecules and Size of nanoparticle. Source [1,3].

From Figure 9 we can see the relationship between the amount of peak shift in LSPR as a function of the number of biomolecules captured on a surface of gold nanoparticles and the size of the Au NP. In order to better understand Figure 9, we plot the individual graphs as below for 3 different radii of the Au NP.

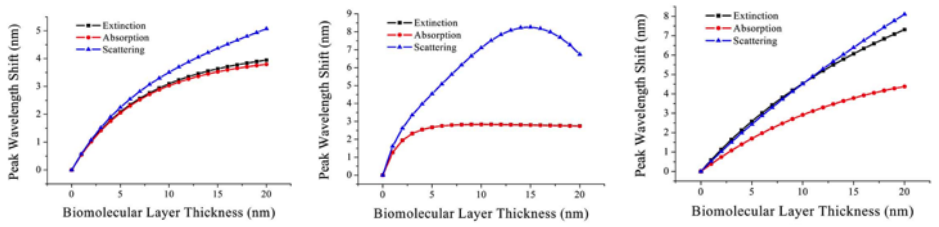

Figure 9a: Peak shift as a function of layer thickness for Au NP of 5nm, 20nm, 50nm

2.3.1 Mie Theory of Localized Surface Plasmon Resonance

LSPR relies on the change in refractive index (R.I.) of the media as a means of sensing bio-particles or pathogens. The key benefits of LSPR also arise from the fact that metal NP like that of gold and silver display a very good UV-Visible absorption spectrum with distinct bands which is not observable in bulk Au or bulk Ag. This method results in wavelength specific absorption of high molar extinction coefficient, typically 3 x 10^{11} $M^{-1}cm^{-1}$ and the Rayleigh scattering has efficiency about 1000,000 fluorophors [17]. The best available analytical model that describes this behavior of nanoparticle is the Mie Theory of the estimation of extinction or (absorbance + scattering).

$$E(\lambda) = \frac{24\pi N_A a^3 \varepsilon_m^{1.5}}{\lambda \ln(10)} \left[\frac{\varepsilon_i}{(\varepsilon_r + \chi\varepsilon_m)^2 + \varepsilon_i^2} \right]$$

In the above analytic model, $E(\lambda)$ represents the sum of absorbance and scattering for any wavelength lambda, known as extinction, N_A denotes the surface area occupied by the Metal-NP of radius 'a', ϵ_m is the electrical permittivity of the surrounding media, which is wavelength independent and real valued (instead of complex valued), ϵ_i and ϵ_r represent the imaginary and real parts of permittivity of the Metal-NP and χ denotes the

spatial resolution, in our case two assuming two Metal NP would be coalesce or aggregate. The above model best represents the various parameters on which the LSPR spectrum would depend on.

2.3.2 LSPR Example using Streptavidin

Streptavidin and biotin interaction is perhaps one of the most well studied and documented pair to understand LSPR. From the graph below obtained from one such study, we see that the peak occurs at about 500- 520 nm, which is characteristic for the peak of Ag NP. The plot denotes the spectrum before adding 9nM of Streptavidin and after the addition of 9nM of streptavidin [1,2,3]. The plot 1 has a peak at 507 nm when it has biotinylated silver nanoparticle whereas peak 2 is the same surface after incubating the sample with streptavidin for 3 hours.

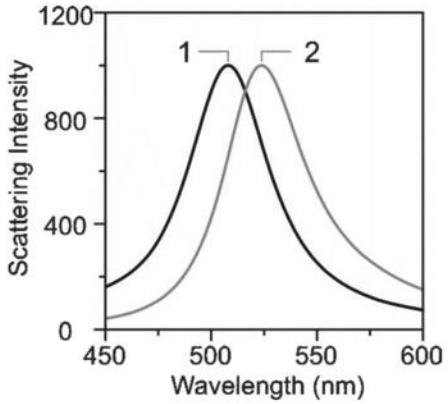

Figure 10: LSPR Plot for biotinylated silver and streptavidin interaction.

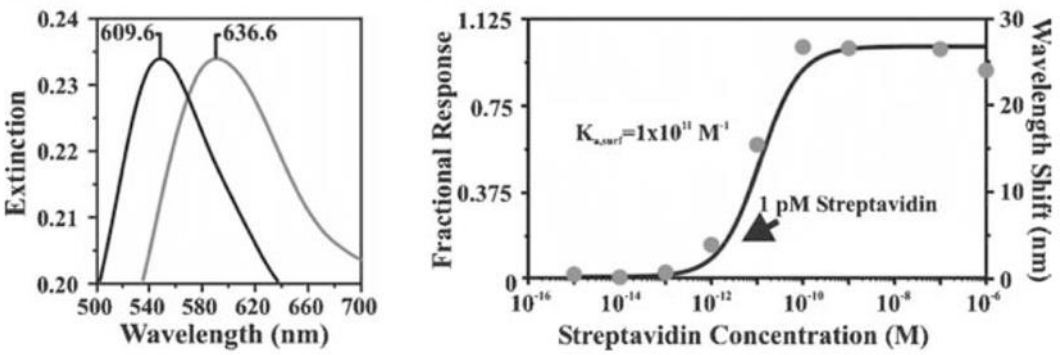

Figure 11: LSPR plot for silver NP with streptavidin and the binding response

In order to illustrate the studies done on streptavidin, we can see from the plot on the left, that the peak is 606 nm before adding SA and 636 nm after adding SA, whereas the curve on the right denotes the SA binding at different concentrations ranging from 10^{-15} M to 10^{-7} M. It is interesting to note that the response of both these platforms can be described by the equation:

$$\Delta\lambda_{max} = m\Delta k \left(1 - e^{\left(-\frac{2d}{ld}\right)}\right)$$

With $\Delta\lambda_{max}$ is the wavelength shift response, m is the sensitivity to refractive index, Δk denotes the change in the R.I. that is created due to the substance adsorbed with thickness d, and ld is the evanescent decay length [1,2,3].

2.3.3 SPR and LSPR

Table 1: Comparison between SPR and LSPR Ref. [18,19,20,21]

Feature	SPR	LSPR
Label Free detection	Yes	Yes
Distance dependence	1000 nm	30nm (size tuneable)
Modes	Angle Shift, Wavelength Shift, Imaging	Extinction, Scattering, Imaging,
Chemical identification	SPR Raman Scattering	LSPR Raman Scattering
Small molecule sensitivity	Good	Better
Refractive Index Sensitivity	2E6 nm/RIU	2E2 nm/RIU
Multiplex capability	Yes	Yes
Field Portability	No	Yes

Comparison between SPR and LSPR is depicted in the above table. As compared, we see that both SPR and LSPR offer label free detection of biomolecules and pathogens,

however SPR has a supreme distance dependence on detection with up to 1000 nm, however LSPR needs the detection distance in the order of 30 nm. Example of surface chemistry done for anti-casein antibody is illustrated in the diagram below. We can see that the deposition of 5nm Chromium and 30 nm of gold layer followed by DDA incubation via a self-assembly in a mono-layer [3].

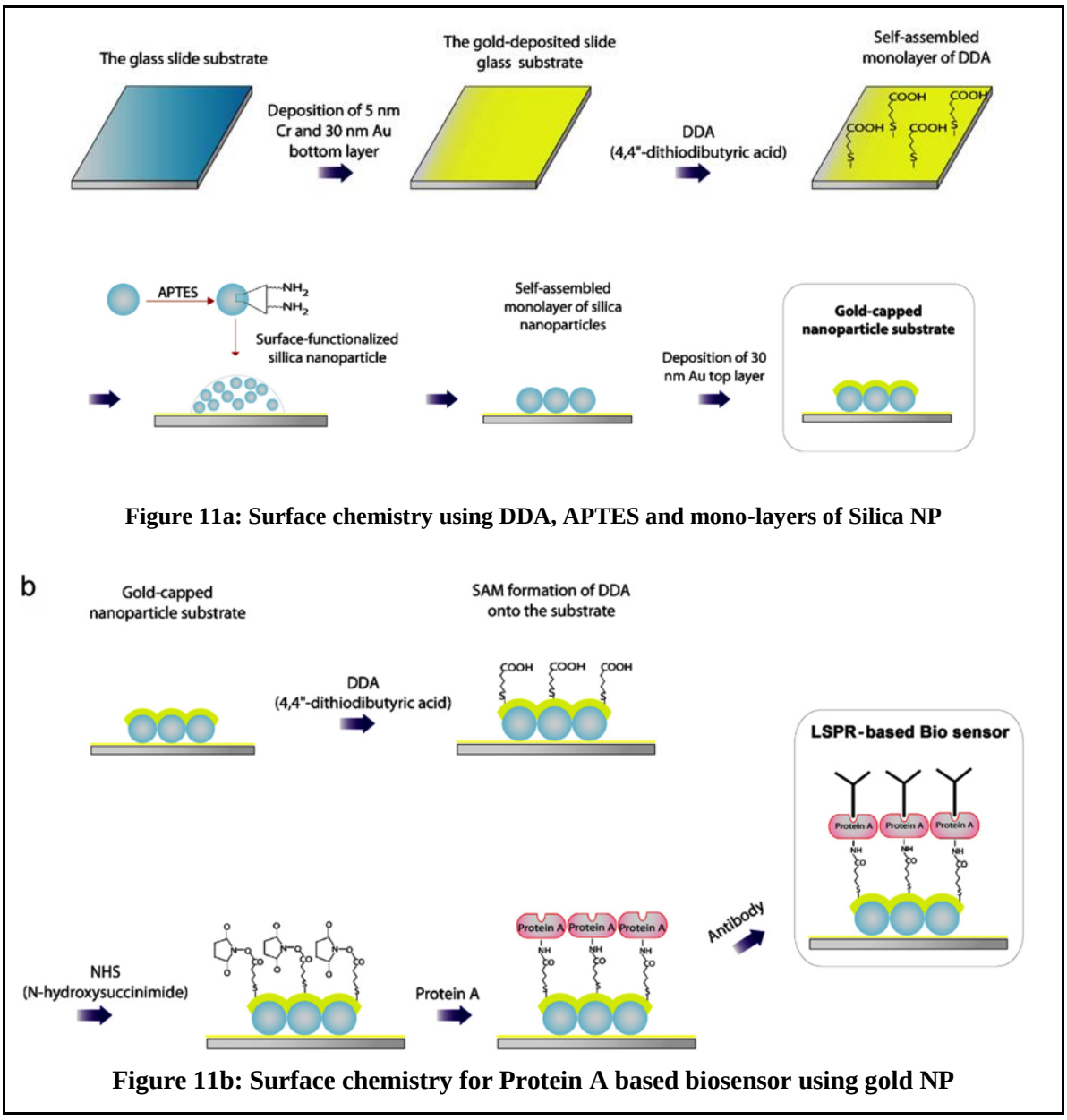

Figure 11a: Surface chemistry using DDA, APTES and mono-layers of Silica NP

Figure 11b: Surface chemistry for Protein A based biosensor using gold NP

The LSPR data obtained from the above set up is shown below. The Atomic Force Microscopy image for the surface shows the surface smoothness when the gold NPs are incubated. The plot on the left however, shows the absorbance peak for gold NP at 550 nm [1,2].

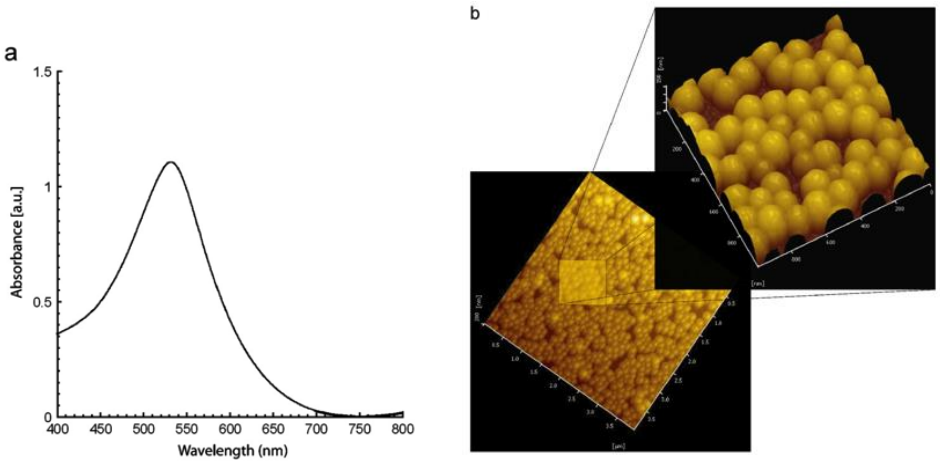

Figure 12: LSPR plot for anti-casein antibody over gold NP and AFM imaging

2.3.4 Surface chemistry

As a preliminary step, after have been functionalized our platform surface with gold nanoparticle, we tested different parameter that characterize the surface chemistry to choose the better combination for starting our experiments.

The aim of this first step is to analyze the sensor response to different buffers parameter such as:

pH, temperature, durability

We start from the comparison between different pH. For this purpose, we prepared Borax NaOH pH=10, PBS pH= 7.4, MES pH= 5. Incubating for:

1hour, 1 day, 2 days, 3 days, 7 days, 14 days, 21 days.

Phosphate buffered saline (abbreviated PBS) is a buffer solution commonly used in biological research. It is a water-based salt solution containing sodium phosphate, sodium chloride and, in some formulations, potassium chloride and potassium phosphate. The

osmolarity and ion concentrations of the solutions match those of the human body (isotonic). PBS has many uses because it is isotonic and non-toxic to most cells.

pH- durability experiment

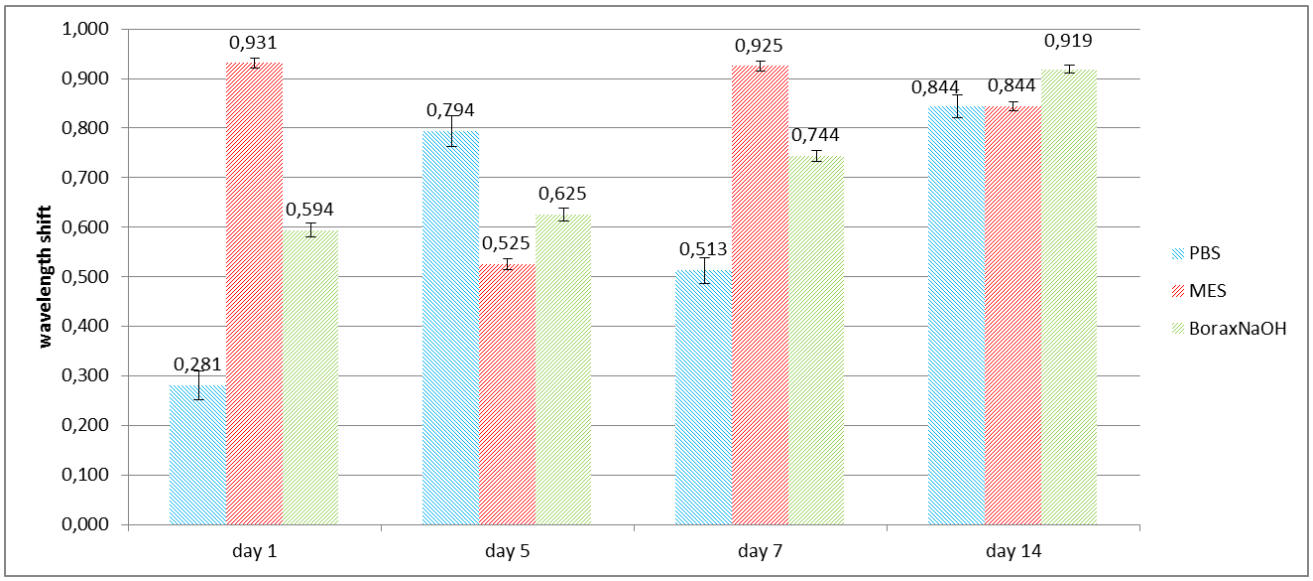

Figure 13 : wavelength shift of 3 different buffer, PBS (pH=7), MES (pH=5), Borax NaOh (pH= 10) after being incubating for 1, 5, 7, 14 days.

From this results we can notice that all the buffers shows a wavelength shift and they can be used from one day till 14 day with no much efficiency difference. So we chose PBS buffer as it is the cheaper and the most common in the literature.

Temperature experiment

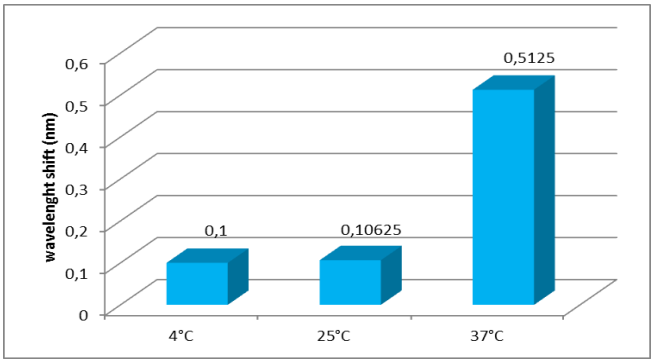

Figure 13a: wavelength shift of PBS buffer in 3 different temperature condition (4°C, 25°C, 37°C)

As the second step we tested different temperature, such as: 4°C, 25°C, 37°C and we used room temperature as a control. We can clearly see that PBS have a very small wavelength shift, so that we choose to use the buffer at 37°C to have a more detectable peak.

Chapter 3

Detection of *Escherichia coli* using Lab-on-a-chip platform

Disease causing agents, like *E. coli*, dengue virus, HIV, HBV, etc. are a grave cause of concern in today's time of growing healthcare costs. Health ailments like that arising from contaminated food sources, injuries that attract infections, such sepsis or growth of other pathogens. It has become very important and vital to reduce associated healthcare cost by detecting these pathogens and other disease causing agents at early stage in resource constrained settings. The present state of the art techniques that involve Polymerase chain reaction (PCR and its variants like RT-qPCR, qPCR, etc.) or agar plate culture for processing samples has the main drawback of high cost, large processing time, technical expertise and lack of deploy ability at the point-of-care. This challenge is still being address by the biomedical research community and much work can still be done to overcome such challenges. In this chapter we describe a low cost POC method of detecting *E. coli* in clinically relevant conditions [9] like Phosphate buffered saline, whole milk, dietary spinach, and whole blood from patients. We use a immunoassay based microfluidic chip to capture these pathogens and then enumerate them with high accuracy and reliability. The results indicate that there is close to 70% capture efficiency for the bacteria in PBS solution when using LPS binding protein. It must also be noted that PBS, whole blood, and milk samples had a very detection cut off close to 50 Colony Forming Unit (CFU) per mL, however, with spinacia oleracea (common spinach) the limit of detection was as high as 500 Colony Forming Unit (CFU) per mL. The work done by researchers at the Bio-Acoustics MEMS in Medicine Laboratory at the Massachusetts Institute of Technology and Harvard Medical School is focused on using such novel technologies for developing POC device for detecting multiple pathogens using MEMS and microfluidic platforms. According to the United States Center for Disease Control (CDC), sepsis is one of the most lethal health condition that has a mortality rate as high as 29% to 49.78% as of 2013. Sepsis is categorized as a whole body condition in response to any infection, also known as "Systemic Inflammatory Response Syndrome" a.k.a. SIRS in the medical community. Organ failure, high lactose content in blood, increased amount of bacteria in blood, etc. are just few possible side

effects of a severe inflammatory response. A declining immune system, pyrexia, rashes, low blood pressure, organ failure, are all indication that sepsis is the diagnosis. Most patients who are diagnosed with sepsis are given broad spectrum anti-biotic in response to the bacterial infection. However, a prolonged usage of this medication, causes the bacteria to develop immune response that would make them resistant to the BSAB. There have been many developments in response to developing efficient drugs, early detection using appropriate biomarkers, etc. for sepsis, however, the number of people who are dying of sepsis each year has been increasing if not stabilizing at a constant value. The CDC predicts that roughly 75.9 million people are affected by food borne pathogens and vectors, leading to more than 300,000 emergency hospitalization cases and close to 4780 deaths every year. Other organs within the United States, like the DOA have reported that the annual loss to the US government from pathogens from food sources, like *E.coli* is approximately $ 6.778 billion. Almost two years ago, in 2011 Shiga toxins belonging to Stx1 and 2 from the lambdoid prophages, caused by *E. coli* were a cause of global concern. It is believed that these Shiga toxins block the protein synthesis pathways in the host cell or the target. They enter the host through a macropinosome and once inside the host, they behave like N-Glycosidase protein where they break a specific adenine bond in the mRNA, thus stopping protein production [9].

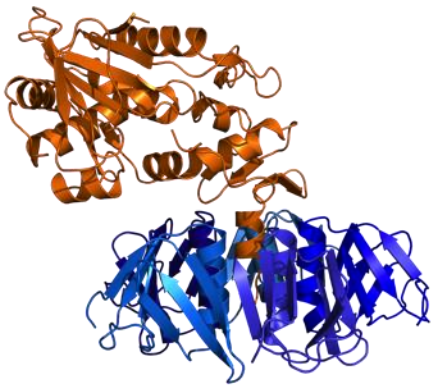

Figure 14: The chemical structure (Ribbon diagram) of the Stx1 and Stx2 toxins. Ref [18]

It has been reported that Sepsis is the 10th leading cause of mortality resulting in about 25,000 deaths over a study period of seven years in 48 hospitals in the United States. These data show that the early stage detection of *E.coli*, the main causative agent of sepsis, is very important.

The present technique of Agar plate culture is the most reliable method and often coined as the gold standard for detecting pathogens like *E.coli* from various food samples.

Figure 15: Agar plate culture sample in RBC for pathogen detection. Ref [18]

In order to compare how traditional methods like agar plate culture using MacConey agar plate versus a MEMS based platform for detecting *E. coli* we use the below flow chart to illustrate the time difference in the two methods [9].

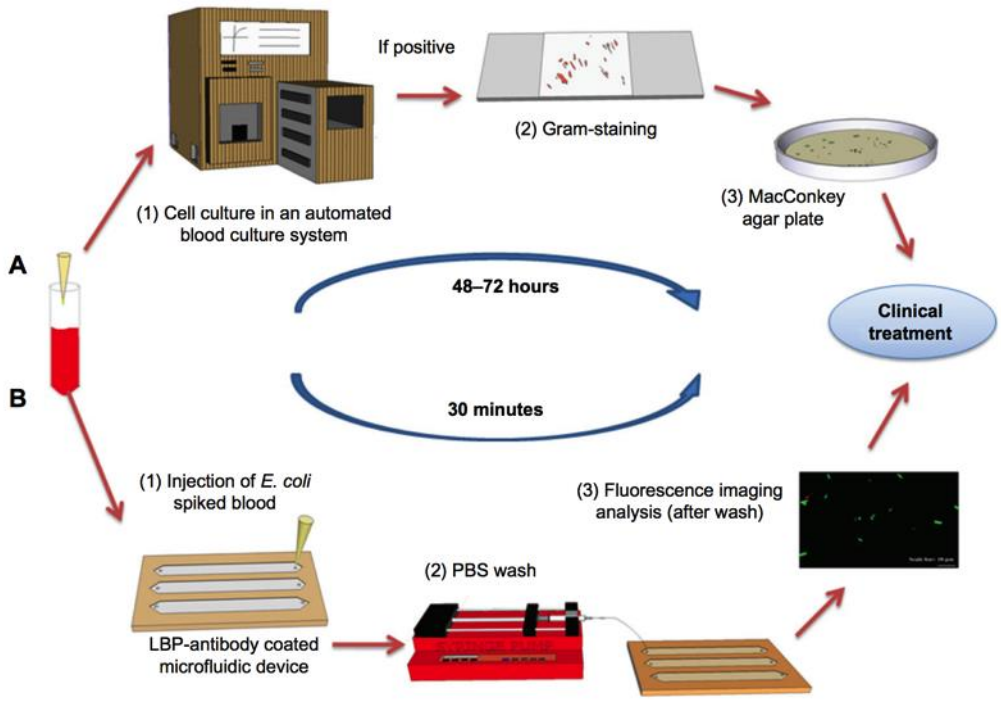

Figure 16: Gold standard agar plate culture compared with MEMS platform Ref. [9]

One of the important challenges in agar plate culture is the need for a minimum amount of sample to culture, this lack of minimum leads to false positive results from 7.09% to 21.06% as per data from United States CDC. From the above illustration of the process flow of agar plate culturing we see that there is need for clinical expertise to perform the Giemsa staining (The stain is a composite of Methylene Blue, Eosin and Azure B) followed by MacConkey plates and the duration of this process if almost two to three days. On the contrary, when we see the MEMS based method, there is no need for any large instrumentation set up. As previously indicated, both RT-qPCR and ELISA methods need large device set up or multiple steps to prepare and wash the sample, all which are time and capital intensive. In the method described above, which takes about half an hour, we need to inject *E. coli* in blood sample into the channels of the microfluidic device. The surface chemistry of the device has lipo-polysaccharide binding protein anti-body, which is then washed with Phosphate buffered saline using a injection machine and then the analysis is done using fluorescence imaging. The PBS wash step ensures that any un-captured bacteria are washed away from the surface. In the below figure we describe the micro-fabrication of the microfluidic device using PMMA, DSA and glass slide, forming the chip [9].

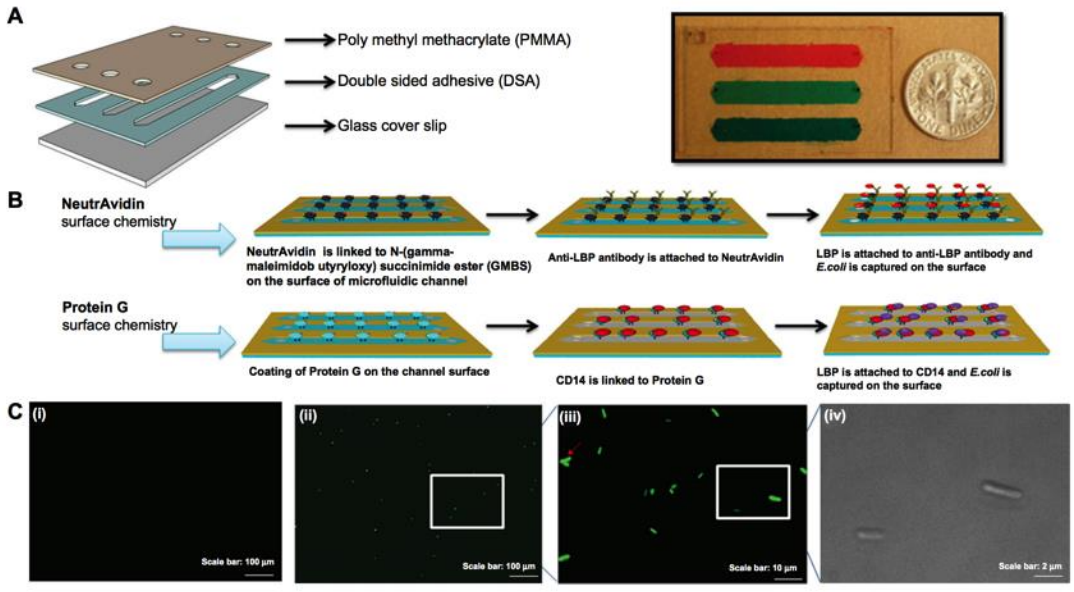

Figure 16a: Device micro-fabrication B. surface chemistry of the channels and c. imaging. Ref [9]

Chapter 4

Nanoplasmonic Detection of HIV

4.1 Introduction

In an effort to have a highly multiplexable platform, we use the method of LSPR to quantitatively detect various intact HIV and its subtypes like A, B, C, D, E, G and panel. In the previous chapter we have seen how *E. coli* can be captured using LBP surface-chemistry on microfluidic channels. We also perform surface characterization using Atomic Force Microscopy when the surface has polystyrene, Poly-L-Lysine, and Gold nanoparticle (AuNP). In the below diagram we illustrate [11] the overall surface chemistry of the LSPR plates for detecting HIV subtypes.

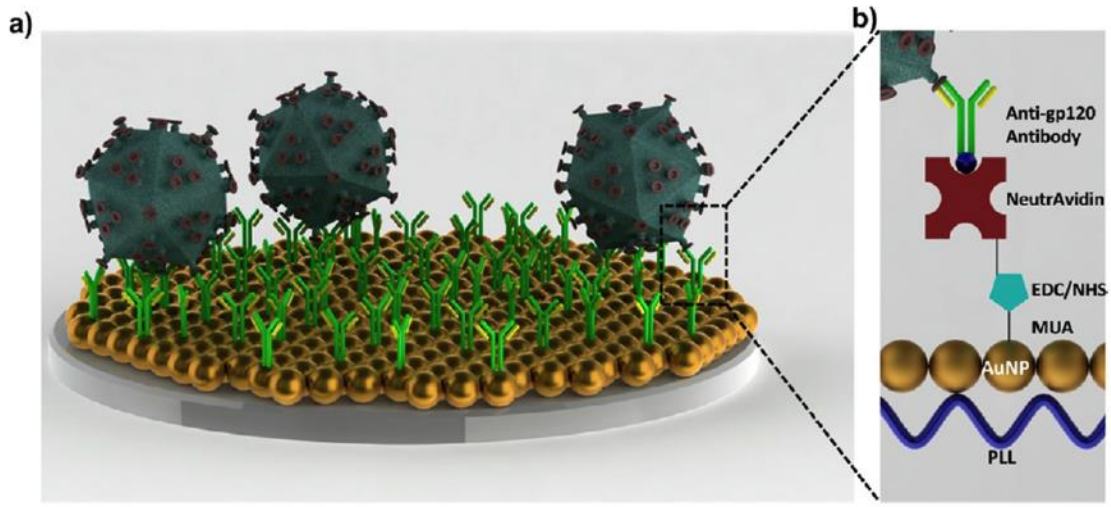

Figure 17a: Overall surface chemistry of the plate, b. specific binding sequence.

In the above figure we see that over a glass slide, a layer of Poly-L-Lysine is coated, on top which, gold nanoparticles have been incubated. This layer serves as the substrate for attaching 11-mercaptoundecanoic acid (MUA) and N-ethyl-N'- (3-dimethylaminopropyl) carbodiimide hydrochloride (EDC)- N-hydroxysulfosuccinimide (NHS) buffer. These

chemicals serve as a binding site for NeutrAvidin (NA) to attach. NA is the last step that holds on to the anti-glycoprotein (gp) antibody that can bind with the HIV Virus [11].

4.2 Materials

The materials used are as follows: Ethanol 200 Proof from Fischer, PBS from Invitrogen, Polystyrene plates from Corning, MUA from Aldrich, EDC from Aldrich, NSA from Aldrich, BSA (Bovine Serum Albumin) from Sigma Aldrich, MES and PLL from Sigma, AuNP from TedPella, NA from Pierce Biotechnology, Biotinylated goat anti-Human Immunodeficiency Virus glycoprotein 120 polyclonal AB was purchased from Abcam. In the below flow chart we describe the surface chemistry in detail [11].

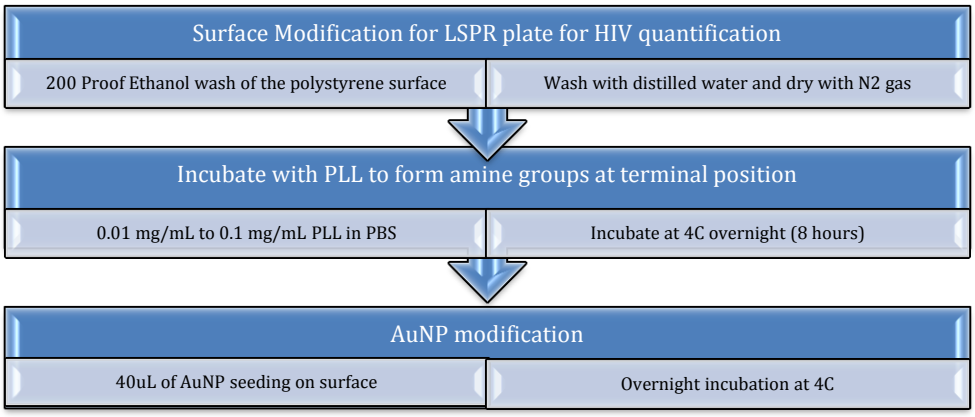

In the above process, we begin by first evaluating if the surface binding of AuNP over the PLL layer is uniform or not, by using a wavelength shift that is a linear function of concentration which was observed as plotted in the below graph. Two incubation times of 24 hours and 72 hours were used to comparison. It was found that there was a statistically same correlation for the two time periods of incubation of PLL concentration ranging from 0.001 to 0.01 mg/mL of PLL in PBS [11].

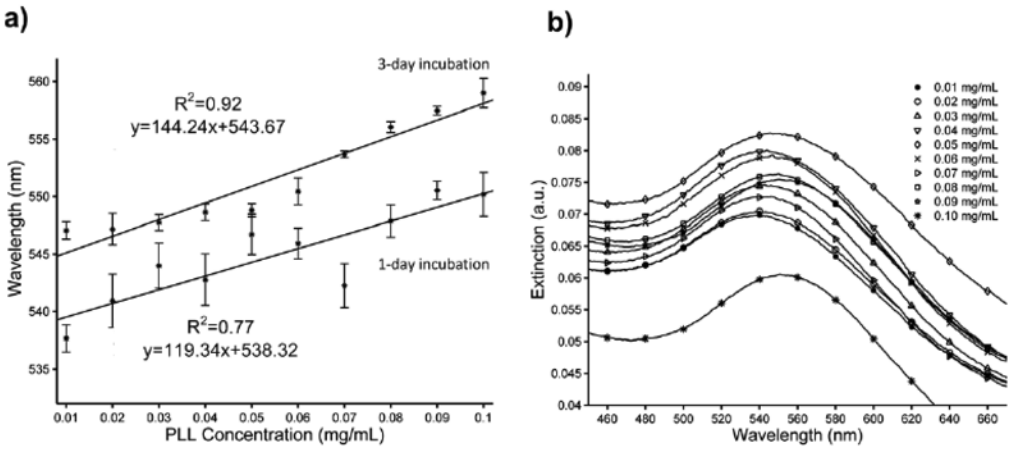

Figure 18. PLL concentration versus Wavelength in nm for 10 different PLL concentration

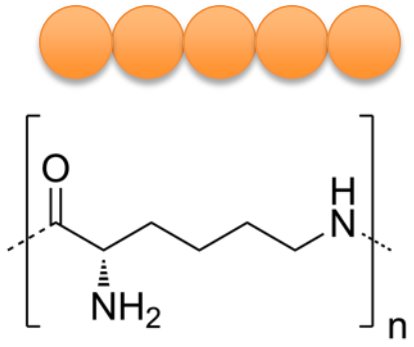

Figure 19. PLL and AuNP binding

From Figure 18 we can see that there a linear dependence on the lambda shift and PLL concentration as it is varied from 0.01 to 0.1mg/mL. Figure 18 b shows the change in extinction coefficient as we increase the concentration of PLL. Antibody surface chemistry and immobilization was carried out following the surface modification using PLL and AuNP. The AuNP layer is incubated with 11-mercaptoundecanoic acid (MUA) in ethanol solution. The reason we use 11mercaptoundecanoic acid (MUA) is to form carboxyl functional groups that can act like a cross-linking agent [11].

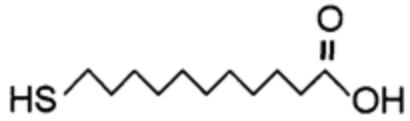

Figure 20: Chemical structure of MUA depicting the Carboxyl terminal group

We then add N-ethyl-N'- (3-dimethylaminopropyl) carbodiimide hydrochloride (EDC) in MES buffer, so that there can be a reaction with the COOH- group to form a amine intermediate.

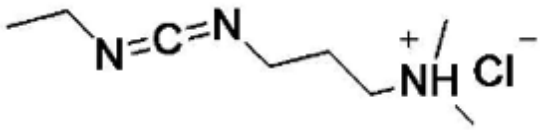

Figure 21: Chemical structure of EDC with amine intermediate group

To this intermediate we add N-hydroxysulfosuccinimide as a stabilizing agent. Following this incubation we add 100uL of NeutrAvidin (NA) with a concentration of 0.1mg/mL so that we can bond AB to the surface. The addition of NA helps to properly align the AB over the surface, thus improving the capture efficiency of the virus. A blocking agent is also incubated, in order to prevent any non-specific adsorption by using bovine serum albumin at 10% concentration and incubated at 39.2 degree Fahrenheit for 60 minutes. After the addition of albumin, we add biotinylated anti-glycoprotein 120 AB to attach to the biotin sites in the NA.

Figure 22. NeutrAvidin from ThermoScientific.

BAMM Labs obtained from the AIDS Research and Reference Reagent Program at the National Institute of Health samples of HIV and its most prevalent subtypes of A, B, C, D , E, G, and strains CRF01_AE and CRF02_AG. These patient samples were from both Uganda and many hospitals within the United States of America and were cultured using

a standard cell culture protocol. Those cells with round nulcei were cultured, a.k.a. Peripheral Blood mononuclear cells, instead of those with lob shaped nucleus. Most cells of the human immune system like, lymphocytes and macrophages are typically PMBC type. Due to the difference in density of various types of cells found in blood, we employ the famous **Ficoll Hypaque density gradient centrifugation (FHDGC)** method to obtain HIV-1 negative cells. Due to lower mass density mononuclear cells and platelets are collected on top after the centrifugation.

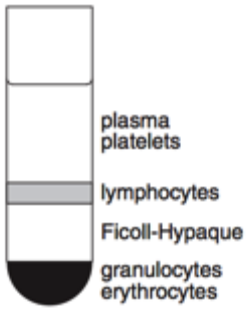

Figure 23: Ficoll Hypaque density gradient centrifugation

After 72 hours, Phytohemagglutinin (PHA), which is a lectin or a carbohydrate binding protein found in plants is stimulated, HIV-1 –ve Peripheral Blood mononuclear cells are co-cultured with HIV +ve Peripheral Blood mononuclear cells, which consist of Roswell Park Memorial Institute (RPMI) 1640 along with L-Glutamine, an essential amino acid and the most freely found amino acid in human blood along with 20% of fetal bovine serum which is obtained from blood after natural coagulation- FSA also contains a majority of BSA by content, penicillin obtained from the penicilium fungi, streptomycin- the remedial drug for Tuberculosis (TB) , (4-(2-hydroxyethyl)-1-piperazineethanesulfonic acid) (HEPES) buffer and recombinant human interleukin-2 (IL-2) which helps in the proliferation or increasing the number of T-cells as an immune response is used during cell culture. The entire cell culture was performed under 5 percent of carbon dioxide atmosphere at 37 degree C and there was bi-weekly replenishments of the cell media. 72 hour PHA stimulated HIV-1 +ve Peripheral Blood mononuclear cells were added every seven days and the supernatant was taken for p24 antigen test, which is done as a standard test for HIV detection. In the below diagram we illustrate the detailed structure of an HIV [11,12]

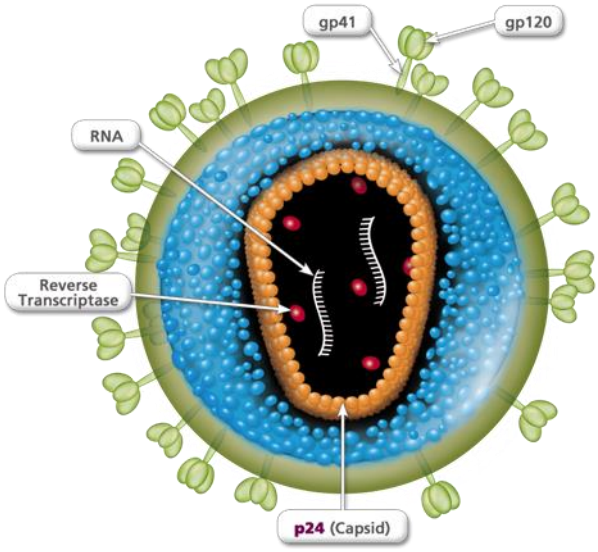

Figure 24: Human Immunodeficiency Virus

Using the above-mentioned protocol for cell culturing, different subtypes of HIV were cultured in PBMC.

4.3 Experiment

We collected HIV infected patient blood samples from the Massachusetts General Hospital. Before spiking whole blood with HIV, we performed a reverse transcriptase quantitative polymerase chain reaction test to quantify the amount of various HIV subtypes. The following dilutions were made: HIV A subtype of 6.55 E8 copies/mL, Subtype B of 6.37 E8 copies/mL, Subtype C of 20.9 E8 copies/mL, Subtype D of 7.00 E8 copies/mL, Subtype E of 8.39 E8 copies/mL, Subtype G of 6.53 E8 copies/mL, HIV Panel of 14.80E8 copies/mL. Guanidine Isothiocynate was used for lysis to extract RNA for HIV stock quantification [11].

Figure 25: QIAamp Viral RNA Mini Kit

4.4 Results

After the viral load quantification using the RT-qPCR, stock solutions of HIV- A, HIV-B, HIV-C, HIV-D, HIV-E, HIV-G, HIV-Panel were spiked into whole blood serum so that the final concentration cab range from 50 to 1 million copies per mL. 100uL of HIV spike whole blood was pipetted into each surface modified wells and left for incubation for 60 minutes at 39 degree F. The control group was whole blood without any HIV spiked into it [11].

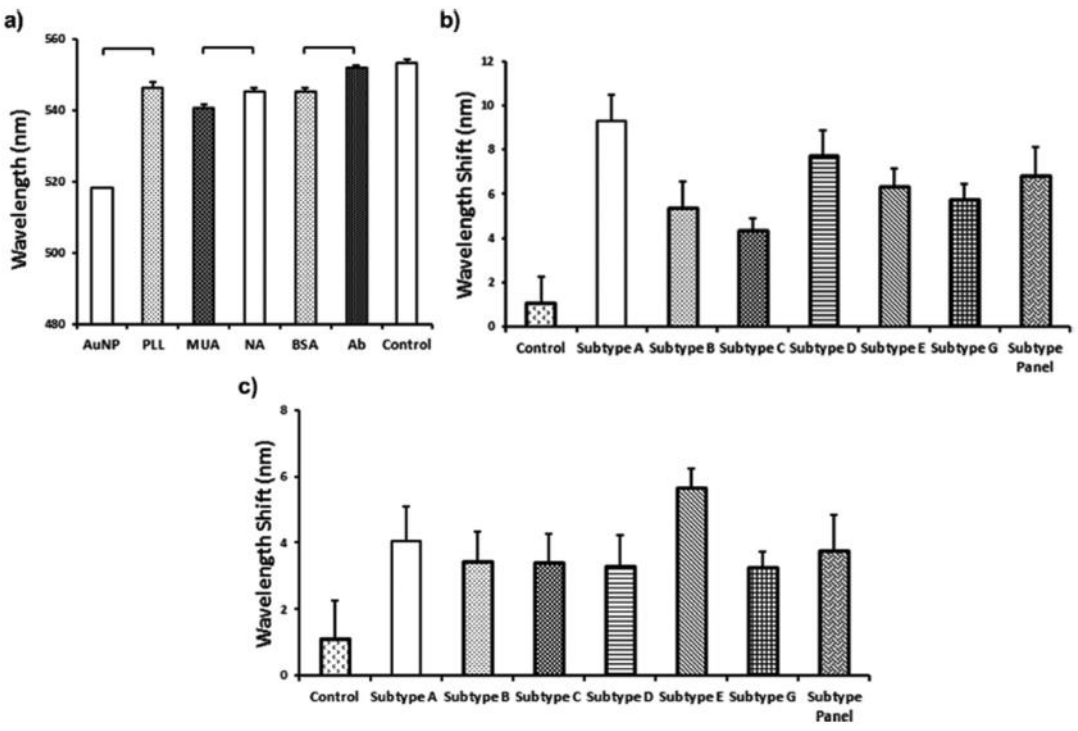

Figure 26 a. Wavelength peak for each surface modification b. Wavelength shift (nm) after HIV spiking c. Limit of detection for each HIV subtype [11].

In order to make measurements using the Varioskan, after each step of the surface chemistry we wash the wells three times each with 100 uL of Phosphate buffered saline and then add PBS fourth time for making the measurement. This is a standard protocol while performing the surface chemistry. For every HIV subtype (A, B, C, D, E, G, Panel), we subtract from the corresponding control group spectra, to get the shift in wavelength before and after HIV spiking and the change in extinction intensity +/- standard error of mean (SEM). Another set of separate Reverse transcriptase quantitative polymerase chain reaction was also performed to reduce any dilution errors. We use a fixation solution of Paraformaldehyde (PFA) before the HIV detection step over the captured virus. From figure 26a. we see that Au has a peak at 518 nm and when we incubate AuNP over PLL, the peak is shifted to about 546 nm and all the other layers starting from MUA, ED/NHS, NA, AB gave a peak shift to 552 nm [11]. When control (no HIV blood sample) was added, there was no significant or observable peak shift. Figure 26b shows the peak shift when HIV infected samples are added. The

corresponding values displayed on the graph are: 9.3 +/- 1.2 nm for Subtype A, 5.4 +/- 1.1 nm for Subtype B, 4.4 +/ 0.5 nm for Subtype C, 7.8 +/1.1 nm for Subtype D, 6.3 +/- 0.8 nm for Subtype E, 5.8 +/- 0.7 nm for Subtype G and finally 6.9 +/- 1.2 nm for Subtype Panel of HIV. Figure 26c shows us the lower limits of detection and the corresponding peak shift of wavelength. For HIV subtype A, B, C, D, E, G and panel the following lower limits of detection in copies/mL were obtained: 1346, 10609, 14942, 98, 120159, 404 and 661.

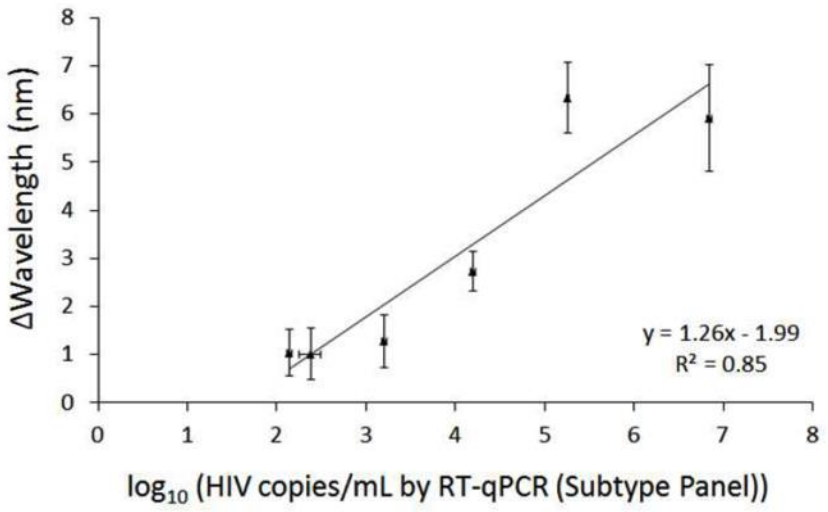

Figure 27: RT-q-PCR quantification and the obtained wavelength shift in nm.

From the above plots we see that the lowest limit of detection by the Reverse transcriptase quantitative polymerase chain reaction, which is considered the gold standard method, the value is about 50 copies/mL. Any result that was below this lower threshold was also reported as 50. After the above measurements were done, surface characterization was also done using atomic force microscopy. In order to better understand the physics and working of a scanning force microscope, we use the below illustration Figure 28. The AFM has a spatial scanning resolution of 5 um x 5um, that can be used to analyze the surface roughness. After performing the first two surface modification on polystyrene by adding Poly-L-Lysine [11] and AuNP the surface roughness changed 18.93 +/- 1.35 nm. It must be noted that this value is the root mean

square value over multiple random 5x5 um surface samples, and the analysis was done using the non-parametric Kruskal Wallis one way ANOVA.

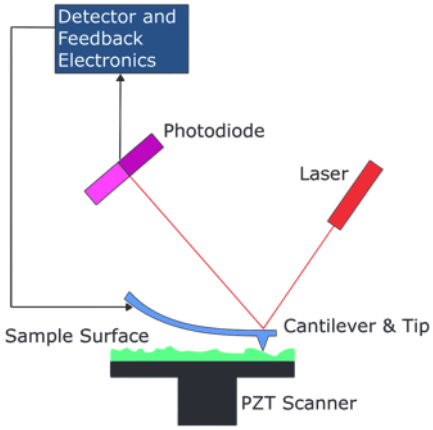

Figure 28a. Working of Atomic Force Microscope for surface characterization in LSPR platform. Ref [19]

In order to make the measurements we used the Asylum-1 MFP-3D AFM system which has been depicted below.

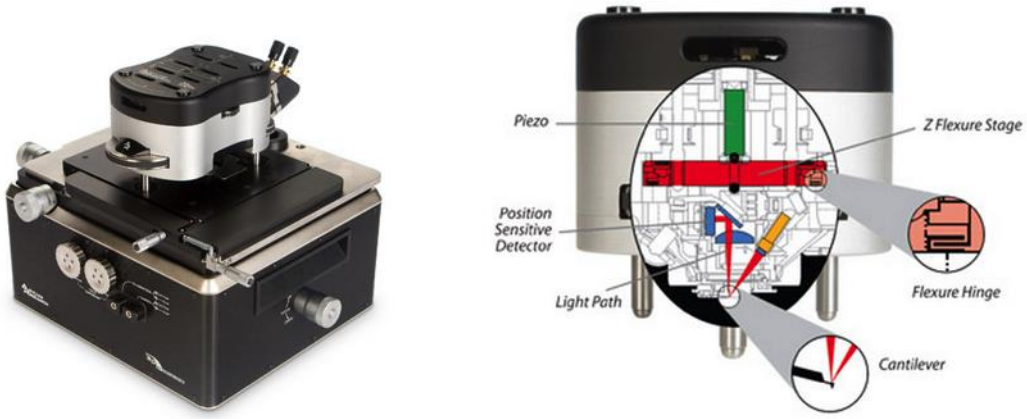

Figure 29a. Asylum MFP-3D Atomic Force Microscope. Ref [19]

The surface roughness before the PS surface was modified with PLL was observed to be around 2.50 +/- 0.10 nm RMS. When we incubated the surface with Poly-l-Lysine overnight at 4 degree C, the roughness changed to 2.40 +/- 0.20 nm, which is a very small difference in the RMS roughness. However, after we incubate AuNP overnight at 4 degree C, the surface roughness increased to 4.70 +/- 0.2 nm. For (n=8, p > 0.005) indicated that there is no statistically significant difference, however for (n=8, p< 0.005) is statistically different for AuNP modification. The uniformity of coating was computed using Image-J software with a value of 83% on the LSPR platform. This implies that 24 hour incubation of PLL followed by AuNP [11] gave a very dense coating which was needed for further surface modification. After the surface were modified, we incubate the platform at 39 degree F and there was no coffee ring effect observed, which is otherwise seen when liquids evaporate from a surface and leave a stain mark behind.

After performing surface roughness estimation using the AFM, we also perform a **Scanning Electron Microscopy** of the HIV that was captured using the LSPR platform. Each polystyrene well had a surface area of approximately 4 million square microns. After the surface modification was done using MUA, EDC/NHS, NA, AB [11] we imaged the surface using SEM at 4.7 mm working distance and 4000 volts of exciting voltage.

Numerical estimation and theoretical modeling of the HIV capture over surface modified Polystyrene. From the research published by Decuzzi et.al [7], we obtain the following mathematical models:

$$N = V \times C \times \frac{A_b}{A} \times \mu \times \frac{\kappa^2}{\mathrm{K}^2}$$

$$\mu = \pi r_0^2 \exp\left\{-\frac{\lambda}{Tk_b}\left[6(a\gamma^{-1} + \delta_{eq})F^s + 8\frac{a^2}{r_0}T^s\right] \times \frac{a}{r_0 \times r_0}\frac{S\mu}{m_r}\right\}(m_r m_l K_a^0)$$

$$F^s = 1 + (1.7360 - 0.1380\gamma + 0.1280\gamma^2 + 0.09\gamma^3)\exp(-\gamma)$$

$$T^s = 1 + (-20.50 - 46.50\gamma - 35.10\gamma^2 + 8.95\gamma^3)\exp(-\gamma)$$

In the above expression, N denotes the number of AuNP that are on the active area of consideration, V is the volume in milliliters of the of the Virus solution in blood and V= 0.1 mL, C is the number of copies of the HIV present per milliliter ranging from 50 to 10^6, A_b is the beam area of the scanning optical beam of about 3.1 mm^2, A is the entire surface area of the Polystyrene well of about 37 mm^2, μ denotes the capture efficiency of the HIV and its subtypes which is typically greater than 70%, $\frac{\kappa^2}{K^2}$ is the ration of surface area of HIV (kappa) to that of AuNP (K). The notations $m_r \ and \ m_l$ are the receptor and ligand mass density, whereas K_a^0 represents the association constant of the virus over the surface modified PS at no load condition of receptor-ligand pair. The shear mechanical stress experienced at the walls is denoted by $S\mu$; F^s and T^s are the coefficients that depend on the shape of the ligand. The bond length that is formed between the ligand and the receptor is denoted by $\lambda = 0.1\ nm$. The Boltzmann constant is represented using k_b and the half-length of the HIV is represented by the letter 'a', δ_{eq} is the separation between the virus and the antibody coated surface at thermal equilibrium, r_0 is the radial length of the Virus, γ denotes the aspect ratio of the virus = 1, which is defined as the ration of half length a to b of the major and minor axes. T= 300K is the temperature and m_l and K_a are not numerically known for the virus. From the experiments performed [11], we obtain a value for μ as 70% to 78% when the blood is spiked with HIV, for the microfluidic chips with surface chemistry as described previously. The data obtained from experiments on the number of virus captured, fits well with the above model described.

We also summarize the data obtained by the experimental maximum data method in the below table. The results were also corroborated, by taking patient blood samples with those infected with HIV, we took n=8, and used the LSPR platform to determine [11] the corresponding peak shifts in the samples. The highest peak was given close to 2.8 nm at 3900 copies/mL and the lowest peak was at 1.3 nm for 481 copies/mL

Table 2: HIV Subtype compared with corresponding maxima and minima peaks

HIV Subtype	Highest Peak	Highest Concentration (copies/mL)	Lowest Peak	Lowest concentration (copies/mL)
A	5.2 nm	6.5E05	1.3 nm	50
B	4.7 nm	8.3E05	2.5nm	89
C	6.3 nm	1.3E06	2.7 nm	50
D	4.3 nm	3.8 E06	1.7 nm	98
E	4.7 nm	1.3 E06	1.2 nm	50
G	4.8 nm	1.1 E06	2.0 nm	404
Panel	6.5 nm	2.9 E06	1.5 nm	101

The proposed LSPR platform can only be deployed in resource constrained setting if it has a proven high repeatability and reliability.

In order to compute these important parameters we define the below mathematical expression:

$$Repeatability = \frac{Mean\ of\ wavelength\ shift\ per\ concentartion}{Mean\ of\ Wavelength\ Shift + SEM\ per\ concentartion} \times 100$$

Using the above equation [11], we compute the repeatability for different concentrations ranging from the minimum copies/mL to the maximum copies/mL and has been summarized in the below table.

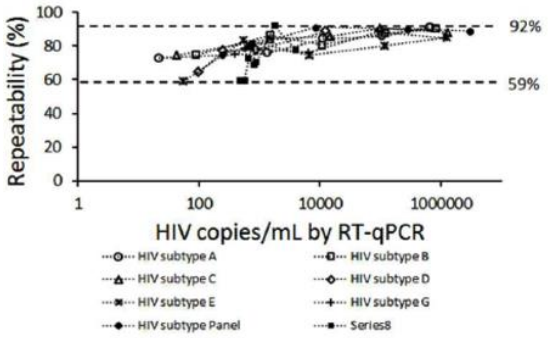

Figure 30. Repeatability plot. Ref [11]

HIV Subtype	Repeatability	Highest concentration (copies/mL)	Lowest concentration (copies/mL)
A	72 – 90%	6.5E05	50
B	74.9- 89.9%	8.3E05	89
C	75-87.9%	1.3E06	50
D	64-90%	3.8 E06	98
E	59-85%	1.3 E06	50
G	74.9-83.9%	1.1 E06	404
Panel	74.9-88.9%	2.9 E06	101
Patient Sample	59-77.9%	3910	481

The repeatability factor was computed for the wavelength shifts for the various subtypes of HIV under consideration at different concentrations ranging from minimum 50 copies to E05 copies/mL. The plot in Figure 30 shows that the values lie between 59% to about 91.9% for various copies/mL values of HIV spiked blood [11] and patient blood obtained from the Massachusetts General Hospital.

By utilizing the method of mathematical curve fitting we can use this data to compare with actual HIV infected patient blood samples. The quantitative enumeration is possible using the extinction intensity analysis by this method. In the below figure, we see than patient blood sample [11] (whole blood) are evaluated using LSPR platform. From this method the value reported was from 2.2 log base 10 copies/mL to 3.69 log base 10 copies/mL in patient samples. The same blood sample when analyzed using Reverse Transcriptase quantitative polymerase chain reaction, report a viral load of 2.69 log base 10 to 3.59 log base 10 copies/mL. In the adjacent figure below, Bland Altman ANOVA between the LSPR platform and Reverse Transcriptase quantitative polymerase chain reaction method based counting are shown, and the results do not indicate any "systematic bias" in the two methods.

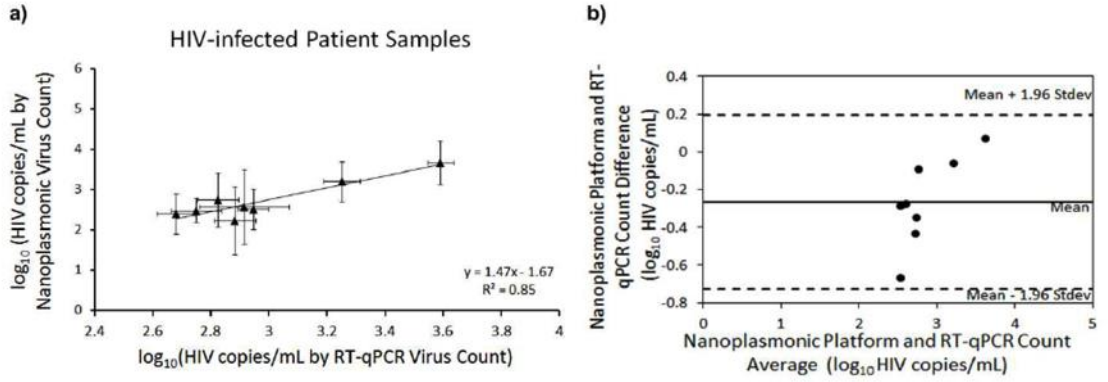

Figure 36: Data from HIV patient samples compared with RT-qPCR and LSPR[11]

In the process of performing the LSPR measurements, we must also be careful about the effect of neighboring NP on the extinction spectrum obtained. In recent papers, it has been reported that the arrangement of AuNP can create some regional hot spots where the

SPP can be amplified due to very small inter-NP distance. Such amplifications [11] can also be used in the detection of Adenovirus which is about 100 nm is size and are double stranded DNA viruses unlike HIV. The effective refractive index also affects such a detection mechanism.

4.5 Remarks

Before analyzing the data from curve fitting method and experimental data maximum technique the following observations are made [11]:

[1] In the method of curve fitting, the entire spectrum was analyzed due to small wavelength shifts at low concentrations of the HIV. In comparison with experimental data maximum (EDM) method and curve fitting (CF) method, the CF method is more suitable if we use samples having low amounts of virus content[11].

[2] 216 spectral plot [11] with only surface chemistry with antibody (Ab) and 216 spectral plots with the HIV infected patient blood samples after surface chemistry were analyzed. In order to get the difference or the peak shift, we subtract every plot after adding HIV from the control.

[3] 9 out of 216 wells indicated a negative shift of peak, which means that some noise was introduced during the sample preparation step. Such wells were discarded from data analysis [11].

[4] 4 wells had a -1 nm change, which were also discarded from the analysis, due to potential noise from surface chemistry steps [11].

[5] 1 well from 50 and 1 well from 100 copies/mL concentration had a shift larger than the rest from its category + 1 SEM, these two were also rejected.

[6] In case a virus is not trapped on the surface modified LSPR plate, there is no expected shift. However in case of 10 wells, there was shift that was lesser than the device resolution of 1 nm, and thus these 10 were also discarded [11].

Chapter 5

Pathogen detection

5.1 Interferon gamma capture for tuberculosis diagnosis

Tuberculosis (TB), caused by Mycobacterium tuberculosis (MTB), is a major global health problem with an estimated 8.8 million new active TB cases, and approximately 1.1 million deaths in 2011 (WHO, 2011b). Among these new TB cases, the majority occurred in the South-East Asia region, which accounted for 40% of the global incidence. Further, only 65% (5.7 million) of the estimated TB cases in 2010 were reported, indicating the need for improved diagnosis [43]. The WHO estimates that there will be more than 2 million new cases of MDR-TB between 2011 and 2015 (WHO, 2011c). These numbers, combined with increasing spread of infection with multi drug-resistant (MDR), demonstrate an urgent need for new approaches for early diagnosis, therapy monitoring, and disease supervision. Diagnosis of TB infection (active or latent) is essential not only for treatment of the infected individual, but also for controlling its spread among various populations. In TB endemic areas, TB control programs aim to treat active TB patients rather than individuals with latent TB infection (LTBI),which is only evidenced by the immunological responses to MTB proteins [44]. Although LTBI individuals are not infectious, their identification is equally important since 10% of these individuals, particularly the immunosuppressed, can subsequently develop active tuberculosis. The routine diagnosis of active TB infection employs various approaches including smear microscopy, culture of MTB bacilli, detection of MTB nucleic acids (NAATs, nucleic acid amplification tests), and clinical symptoms. Conversely, LTBI is identified via tuberculin skin test (TST) and interferon gamma (IFNγ) release assays (IGRAs). However, current TB diagnosis is limited by three primary limitations:

1) low specificity of clinical diagnosis,
2) unavailability of high performing diagnostic methods in developing world laboratories,
3) incapability to monitor patient compliance to the 6–9 month long therapy.

Although there is an unmet need to develop a simple, inexpensive, sensitive and portable assay for the detection of active MTB infection, and for the differentiation of active TB from LTBI at the point-of-care (POC), where sustainable financial support, laboratory infrastructure, and well-trained operators are limited [40].

Interferon-gamma release assays

IFN-γ release assays have been developed and implemented since 2001 with varying degrees of success (39). These tests measure T cell release of IFN-γ (host cellular immune response) upon stimulation of whole blood with MTB-specific antigens, including early-secreted antigenic target 6 (ESAT6) and culture filtrate protein 10 (CFP10) and TB7.7 (an additional antigen used in modified IGRA kits). IGRA assays are available in two formats, ELISA and enzyme-linked immunospot assay (ELISPOT). ELISA quantifies the concentration of IFN-γ, while ELISPOT test counts the number of IFN-γ-producing antigen-specific T lymphocytes. Although these assays are not affected by prior BCG vaccination as the antigens are absent in all BCG strains, they cannot distinguish individuals having LTBI from those with active disease [41]. In addition, systematic review and meta-analyses have shown that neither of the IGRA assays has better sensitivity than TST in detecting active or latent TB infection in HIV-infected individuals. Thus IGRA assays cannot be used to rule-in or rule-out active TB cases, especially in HIV-infected individuals in high-burden settings. This limitation has led a WHO expert group to discourage the use of IGRA assays for active pulmonary TB diagnosis in low- and middle-income countries. Furthermore, the assay takes 24 h to produce results and requires significant instrumentation and well-trained personnel [45].

How IGRA is performed

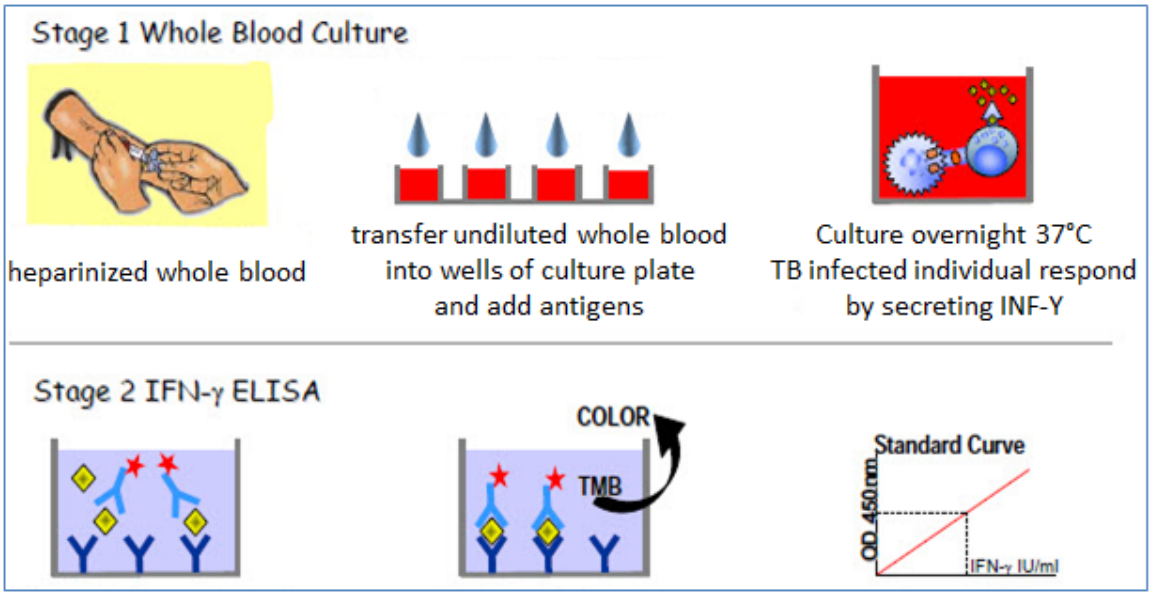

Figure 37: blood cells are incubated with various tuberculosis-specific antigens. In response to the antigens, effector T cells produce interferon-gamma, which is measured quantitatively and qualitatively by either enzyme-linked immunosorbent or enzymelinked immunospot assay

LSPR detection

We have been developed LSPR optical technology also to detect MTB specific antigens (e.g., CFP-10 antigen) in tissue fluid. In this immunobased detection method, monoclonal anti-CFP10 was used as a sensitive TB marker. The biosensing surface, was modified layer-by-layer for antibody immobilization. To modify the surface we have followed the same protocol as for the HIV detection: 0.05mg/ml PLL spiked in PBS, overnight incubation, 50 mL AuNP overnight incubation, 1mM MUA in PBS 3 hours incubation, 191,7mg EDC+ 57,55mg NHS in MES buffer overnight incubation. For the antibody binding we use 100uL of Protein G with a concentration of 0.1mg/mL . The addition of Protein G helps to properly align the Ab over the surface, thus improving the capture efficiency of Interferon γ cytokine. A blocking agent was also incubated, in order to prevent any non-specific binding, by using 10% BSA (bovine serum albumin). Following this incubation we added 100uL of antibody anti-CFP10 that attach with Protein G.

After the antibody incubation the biosensing surface is ready for the interferon gamma detection. As a first step we tried low end measurement, so that we spiked

INF- γ in PBS. Each wells of our plate was filled with different INF- γ concentration, from 1pg/mL to 1fg/ml and for each concentration we added 6 replicates.

In order to get a better value for the detection limit of Interferon Gamma, we decided to repeat the experiment and add more date point to analyze the gap in the graph of extinction intensity vs. wavelength, between the range of 100 fg/ml to 500 fg/ml of IFN-y. We show here an example of the dilution we have done. Using 10pg/ml stock solution of IFN-y, we performed the below dilution steps in order to arrive at the desired concentrations of 100 fg/ml, 200 fg/ml, 300 fg/ml, 400fg/ml and 500fg/ml.

Concentration Dilution Computation: $C_1V_1 = C_2V_2$

10pg/ml × V=500fg/ml × 5ml, → V=0.25 ml of Stock + 4.75 ml PBS, and so on for all the other concentration. We then incubated the plate for 1 hour. Following the incubation, we washed with PBS three times, and allowed the plate to incubate with PBS. We finally analyzed the plate using the **Varioskan Flash** spectral scanning multimode reader. The measuring mode was set to detect Extinction changes per wavelength, swept from 400 nm to 700 nm in steps of 1 nm resolution. This spectral analysis is done for all the 96 wells.

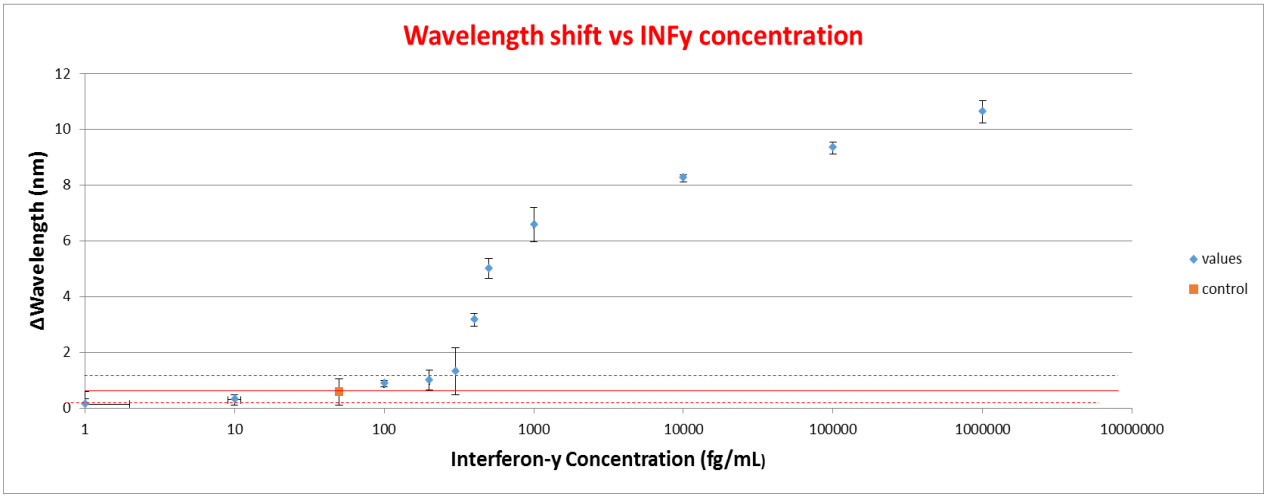

Figure 38: Matlab plot of the wavelength shift peak for different INF-y concentrations analyzed with Varioskan scan.

The above graph represent the wavelength shift of the concentration that we have used to study the platform response. The red area highlight in the plot demonstrates the response of control sample. PBS without IFN-Ɣ was used as a control. All the concentration are referred to the control, those with higher peak shift are the ones we can consider detected by the platform. The platform cannot detect the concentrations with a wavelength shift lower than the control, because they are hidden from the noise. IFN-Ɣ concentrations ranging from 500 fg/mL to 1 ng/mL demonstrate the linear dynamic range of nanoplasmonic platform. The error bars represent mean ± standard errors of the mean (SEM). From this results we can find that the limit of detection for IFN-Ɣ spiked in PBS is 400 fg/ml.

As a final step we spiked interferon gamma in serum with concentration from 100ng/mL to 1fg/ml, the results are shown below.

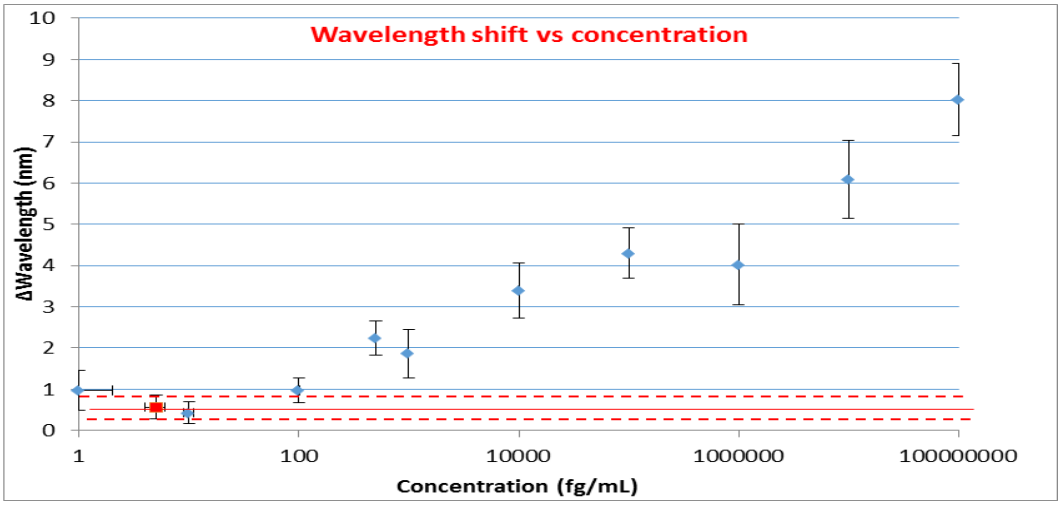

Figure 39: Matlab plot of the wavelength shift peak for different INF-y concentrations spiked in serum analyzed with Varioskan scan.

After analyzing the results we have found the platform limit of detection for INF-y spiked in serum that is 500 fg/ml, while IGRA assay has ng/ml as limit of detection.

In the table below we have summarized the differences between IGRA and LSPR test.

IGRA	LSPR
Time consuming assay (24 h)	Rapid: 1h for incubation and 10 min for analysis
Requirement for pre-processing of blood samples	No requirement for pre-processing
Requires significant instrumentation	Easy to use
Expensive	Inexpensive assay
Limited to Children younger than 5 years old Persons recently exposed to *M. tuberculosis*	Lower limit of detection (down to fg level), so it can be used for Children younger than 5 years old and persons recently exposed to *M. tuberculosis*

LSPR-based immunosensors can also be adapted to sense other antigens and pathogens by altering the detection molecules (e.g., antibodies), thus offering highly versatile platforms. Although LSPR immunosensor offers advantages of simplicity, small sample consumption, label-free, high sensitivity, specificity, and reusability, it requires a well-equipped laboratory infrastructure. Thus, portable and inexpensive SPR-based MTB biodetection systems are needed to minimize laboratory requirement for POC testing. That is why we are trying to improve this platform and make it portable (see chapter 6).

5.2 Kaposi's sarcoma virus capture and detection

Figure 40 kaposi's sarcoma associated herpesvirus

KSHV (kaposi's sarcoma associated herpesvirus **)** is a virus belonging to the family of herpesviruses, which has seven other members that infect humans. Herpesviruses are a group of similar viruses, most of which are extremely common infections that we have probably been exposed to. Some herpesviruses cause diseases while infection with others generally do not cause symptoms. The lay term "herpes" usually refers to herpesvirus type 1, which causes cold sores on the lips (more than 90% of people are infected with herpesvirus type 1), or herpesvirus type 2, which is a sexually transmitted disease that causes "cold sores" on the genitals (about 25% of US adults are infected with herpes type 2). Since both herpes type 2 and KSHV are sexually transmitted (at least in developed countries), they primarily infect adults. KSHV was discovered in 1994 and so, our understanding of it is just beginning. KSHV is different from herpes type 1 and 2 in that it causes a blood vessel cancer called Kaposi's sarcoma (KS), a lymphoma (a cancer of the lymphocyte) called body cavity-based lymphoma and some forms of severe lymph node enlargement, called Castleman's disease. Some early scientific reports suggested that it might also cause multiple myeloma, however, many scientists now believe that this is very unlikely[46].

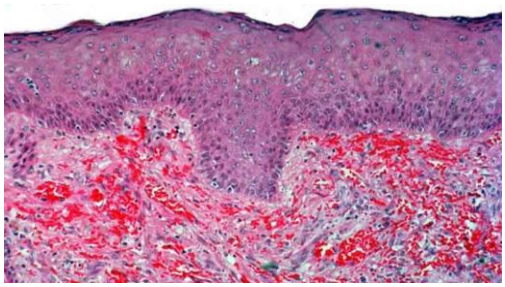

Figure 41 : A photomicrograph of KS in the skin. Blood cell accumulate in the tumor, shown here in red

KSHV is completely different from the HIV virus which causes AIDS, although KSHV-related diseases frequently occur among AIDS patients. The rates of KSHV infection in the general population of Mediterranean countries (Italy, Greece, Israel, Saudi Arabia) are higher than in North America and Northern Europe where KSHV appears to be rare among the general population. In surveys in the UK, France, Switzerland, Denmark and Sweden, the prevalence ranges from 3–7%, also depending on the assay. KSHV prevalence rise dramatically in countries in Southern Europe. In Italy and Greece, prevalence's of up to 35% are found among blood donors, and a marked regional variation has been noted. Antibodies to KSHV are found in 0–29% of the subjects In Africa, in 6–53% of tested samples such as HIV negative patients, antenatal mothers, hospitalized patients and unknown sources. In several respects the global patterns of KSHV infection appear to be similar to those of the hepatitis B virus although we are still at an early stage of understanding the epidemiology of KSHV [47].

Kaposi's sarcoma virus detection with LSPR platform

A major challenge in the diagnosis of KS is the existence of a number of other diseases with similar clinical presentation and histopathological features, requiring the detection of KSHV in a biopsy sample. Infection in immunocompetent individuals results in the generation of pathogen-specific CD8+ T-cell responses that control Kaposi sarcoma herpes virus replication and prevent its progression to neoplastic disease.

We prepared LSPR plate for Kaposi's sarcoma virus infected patients. We functionalized the biosensing surface, for the antibody immobilization following the same step as for the interferon gamma capture. After protein g incubation, we filled half of the plate with 100 µL of 5 µg/mL Antibody **KSHV-HHV.8 ORF K8 1**.A and the other half with **KSHV-HHV.8 ORF K8 1.A/B,** that are mouse monoclonal antibody to lytic cycle. We wanted to try both specific antibody to understand which one is better for our application. The antibody incubation is one hour, after the incubation we washed it 3 times with PBS and the plate is ready for the virus sampling. We have performed the following sampling virus step:

1- Take out all PBS from the wells by pipetting or aspiration. Without touching the bottom of the well.
2- Prepare virus dilutions spiked with PBS and artificial saliva (the artificial saliva receipt is reported in the Appendix B). The concentration range we used was from 10 to 10^6 copies/mL with the following data point:
   10 -20 -50 -100 -10^3 -10^4 -10^5 -10^6 copies/mL.
3- Add 100 µL of each virus dilution to the wells, with 8 sample replicates to minimize the dilution inaccuracies.
4- Seal the plate and its lid with parafilm, and cover with aluminum foil to incubate it at 4°C for 1 hour
5- After the incubation, wash each well with 100 µL of PBS three times, and take out all solutions from each well.
6- Add 100 µL of 3% paraformaldehyde (PFA) in PBS to each well, and incubate it for 10 minutes at room temperature.
7- wash each well with 100 µL of PBS three times and add 100 µL of PBS to each well for the measurements.
8- Before the measurements, the plate is kept at +4C.

We took the measurement with the Varioskan Flash spectral scanning multimode reader. Also for this experiment we set the measure mode to detect extinction changes per wavelength, swept from 400 nm to 700 nm in steps of 1 nm resolution. We present the results in the graph below.

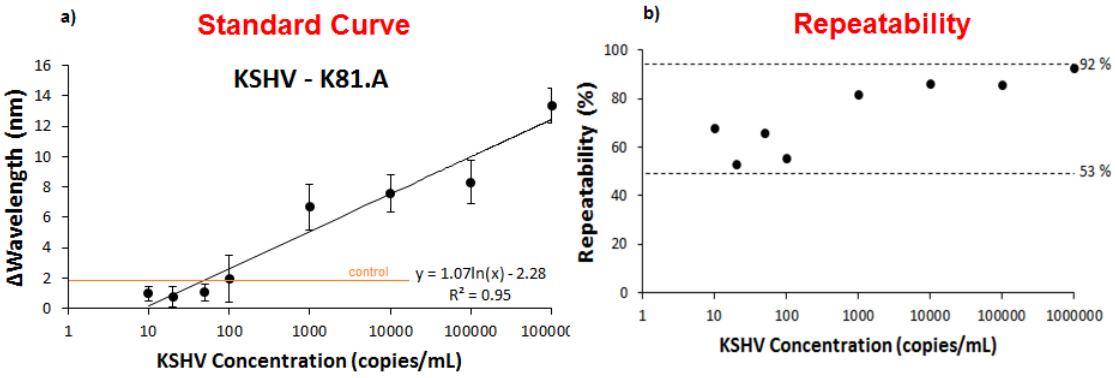

Figure 42 a) Wavelength shift(nm) after virus spiking for each concentration b)repeatability of the measurement for the different concentration.

From this results we can clearly understand that our platform limit of detection is 1000 copies/mL, because lower concentration have a peak shift smaller than the control, that is PBS without virus. We have already define the repeatability in chapter 4, and we have computed it here for the wavelength shifts of the different concentrations ranging from 10 to 10^6 copies/mL . The plot in figure 42 b) shows that the values lie between 53% to about 92% for various copies/mL values. Although the exact number of viral copies per cell has not been determined yet, real-time PCR was recently, used to detect and quantify KSHV, and several reports have demonstrated that number of viral copies varied depending on the disease and its stage. However, to date, only 1 report has used real-time PCR to compare the number of viral copies in samples from KS lesions, and this study was conducted on a limited number of samples. In this scenario our LSPR platform is a good candidate for a Kaposi's sarcoma virus diagnosis.

5.3 Carbamazepine capture for epilepsy treatment

Epilepsy is a brain disorder in which clusters of nerve cells, or neurons, in the brain sometimes signal abnormally. In epilepsy, the normal pattern of neuronal activity becomes disturbed, causing strange sensations, emotions, and behavior, or sometimes convulsions, muscle spasms, and loss of consciousness. During a seizure, neurons may fire as many as 500 times a second, much faster than normal. In some people, this happens only occasionally; for others, it may happen up to hundreds of times a

day. People living with this nerve disorder have seizures that can affect their mental and physical functioning. 2.2 million Americans and 50 million people in the worldwide have epilepsy although there are medicines to treat epileptic seizures nearly one in three patients has a severe side effects from the medicines, these include blurry or double vision, discomfort, fatigue, sleepiness, unsteadiness, and stomach upset [48]. This side effects can be reduced by adjusting drug dosage and timing, using lab test, however these tests can be inconvenient and costly. With our LSPR device we can measure anti-seizure drugs in the blood, that allowed patients and their caregivers to manage their treatment anywhere. By far the most common approach to treating epilepsy is to prescribe antiepileptic drugs. Carbamazepine are the most common anti-seizure medication.

LSPR technique for carbamazepine capture

We prepared the LSPR plate for carbamazepine detection following the same step as before. The antibody used is the Anti-Carbamazepine antibody (ab30435), his target are the carbamazepine. Carbamazepine coupled to BTG through a spacer attached to a 5 carboxamide group and this binding allow us to detect them.

The antibody incubation is 1 hour, after that we washed it 3 times with PBS and we added the carbamazepine spiked in serum with the following concentration range from 0.5 μg/mL to 30 μg/ml. Another hour of incubation and the plate is ready for the measurement that have been taken with the Varioskan scan reader.

The results are plotted in the graph below.

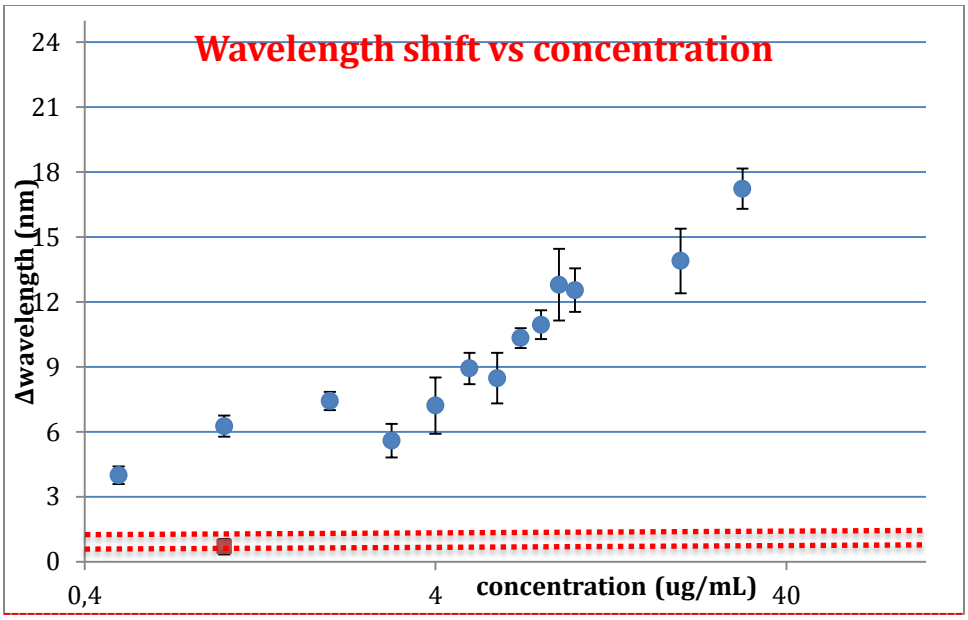

Figure 43: Matlab plot of the wavelength shift peak for different CBZ concentrations analyzed with Varioskan scan

This results clearly demonstrate that the limit of detection of our plate is much lower than the minimum concentration that we are interested in, 0.5ug/mL is the minimum we have tested.

Optimum seizure control in patients on carbamazepine monotherapy is most likely to occur at plasma carbamazepine level of 04-12 µg/mL . The absorption rate of this drug largely change from patient to patient. After oral ingestion, carbamazepine is rapidly absorbed (T-max is formulation-dependent) with a bioavailability of 75–85 %. Its volume of distribution is 0.8–2.0 L/kg, and plasma protein binding is 75 %. The maximum absorption is reached 6 or 8 hours after the drug administration, so that with our platform is possible to detect patient under carbamazepine drugs even after 12 hours from the drug administration. More over carbamazepine is excreted by the kidney and metabolized by the liver and dosages may need to be lowered in patients with liver or kidney dysfunction, even in this case we can detect if the drug concentration in the blood.

In conclusion we can say that innovative solutions utilizing recent advances microfluidic technologies are envisioned to assist the demand for accessible and affordable healthcare for infectious and chronic diseases. This present significant challenges for providing high-value and effective healthcare. Traditional approaches are expanding to include point-of-care (POC) diagnostics, bedside testing, and community-based approaches to respond to these challenges. Highly sensitive and specific lab assays such as cell culture methods, polymerase chain reaction (PCR), and enzyme-linked immunosorbent assay (ELISA) are available for diagnosis of infectious diseases in the developed world. They require sample transportation, manual preparation steps, and skilled and welltrained technicians. These clinical conventional methods provide results in several hours to days, precluding rapid detection and response at the primary care settings. Another diagnostic challenge is identifying multiple pathogens. Our microfluidic platform respond to these challenges. As we have demonstrate it is a rapid assay: 1h for pathogen incubation and 10 min for analysis, easy to use and inexpensive. Moreover until now, there is no general biosensing platform for detection of multiple pathogens, allergens and drugs that can be adaptable to POC settings due to significant technical and biological challenges. Here, we presented a widely applicable platform that can capture, detect and quantify multiple intact viruses including those we analyzed before and we have also tested and verified the efficiency of the platform for Hepatitis B virus, Trichomonas vaginalis virus and Dengue virus.

Chapter 6

Portable Localized Surface Plasmon Resonance

Background

The increasing costs associated with primary health care in developing countries has led to a significant amount of research in the direction of low cost technologies for disease diagnosis that can be used at the point-of-care setting. There are several tecnhieqs that can be used for pathogen detection such as Surface Plasmon Resonance, Localized Surface Plasmon Resonance, Piezoelectric resonators etc. One of the most promising method that has a very sensitivity and reliability in detecting pathogens is LSPR. Present Commercial Off The Shelf (COTS) based devices to perform spectroscopic studies cost about US 40,000 or more. This method of detection is very well suited for clinical settings with considerable infrastructure. However, in order to deploy a detection platform based on LSPR, the primary challenge is to make the device compact and affordable.

Work done

In order to develop microfluidic chips that can be used for multiple disease causing pathogen detection at the point-of-care using the method of LSPR, there is however an unsaid need for the LSPR Scanning reader. As depicted in Figure 44, this device is neither portable nor affordable, for it to be deployed in resource-limited settings.

Figure 44: Varioskan LSPR reader, costing USD 42,000/-

In order to overcome this barrier, we have developed and designed a portable version of the same Varioskan Scanning mode reader with a simple optical set up.

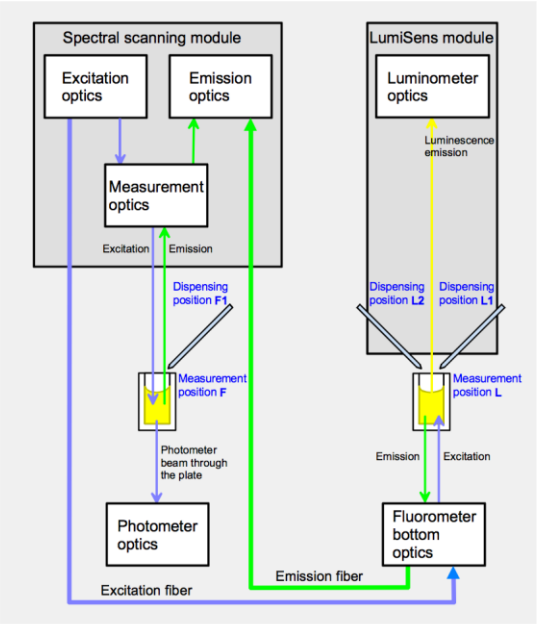

Figure 45: The Photometric scanning mode, operating physics.

The proposed system has the three following basic components: Light source, Chip analyzer, Spectrometer.

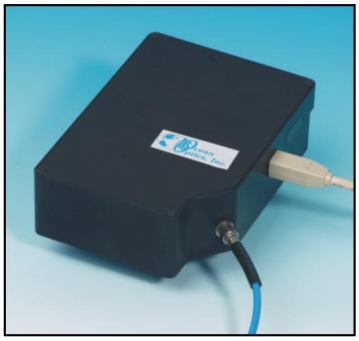

Figure 46: Components of a Portable version of LSPR b: High resolution spectrometer .

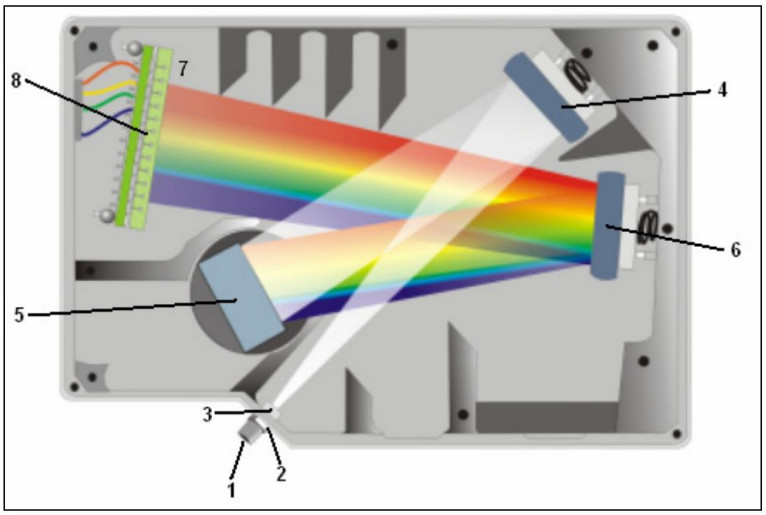

Figure 47: Components of the Spectrometer

The description of each component shown in Figure 40 has been elaborated below in TaBle A1.

Item	Name	Description
1	**SMA Connector**	The **SMA Connector** secures the input fiber to the spectrometer. Light from the input fiber enters the optical bench through this connector.
2	**Slit***	The **Slit** is a dark piece of material containing a rectangular aperture, which is mounted directly behind the SMA Connector. The size of the aperture regulates the amount of light that enters the optical bench and controls spectral resolution. You can also use the HR2000 without a **Slit**. In this configuration, the diameter of the fiber connected to the HR2000 determines the size of the entrance aperture. Only Ocean Optics technicians can change the **Slit**.
3	**Filter***	The **Filter** is a device that restricts optical radiation to pre-determined wavelength regions. Light passes through the **Filter** before entering the optical bench. Both bandpass and longpass filters are available to restrict radiation to certain wavelength regions. Only Ocean Optics technicians can change the **Filter**.
4	**Collimating Mirror**	The **Collimating Mirror** focuses light entering the optical bench towards the Grating of the spectrometer. Light enters the spectrometer, passes through the SMA Connector, Slit, and Filter, and then reflects off the **Collimating Mirror** onto the Grating.
5	**Grating***	The **Grating** diffracts light from the Collimating Mirror and directs the diffracted light onto the Focusing Mirror. **Gratings** are available in different groove densities, allowing you to specify wavelength coverage and resolution in the spectrometer. Only Ocean Optics technicians can change the **Grating**.
6	**Focusing Mirror**	The **Focusing Mirror** receives light reflected from the Grating and focuses the light onto the CCD Detector or L2 Detector Collection Lens (depending on the spectrometer configuration).
7	**L2 Detector Collection Lens***	The **L2 Detector Collection Lens** (optional) attaches to the CCD Detector. It focuses light from a tall slit onto the shorter CCD Detector elements. The **L2 Detector Collection Lens** should be used with large diameter slits or in applications with low light levels. It also improves efficiency by reducing the effects of stray light. Only Ocean Optics technicians can add or remove the **L2 Detection Collection Lens**.
8	**CCD Detector (UV or VIS)**	The **CCD Detector** collects the light received from the Focusing Mirror or L2 Detector Collection Lens and converts the optical signal to a digital signal. Each pixel on the **CCD Detector** responds to the wavelength of light that strikes it, creating a digital response. The spectrometer then transmits the digital signal to the OOIBase32 application.

Table A1: Description of sub-components of the Spectrometer

We used the Portable LSPR device to take measurements for the chips. We used a chip that had been incubated with Gold NP. Initially our results had a very large deviation from the expected absorbance spectrum for Au NP, due to a calibration problem. The original calibration had a dark region in the light source, indicating that the source light was not properly adjusted. This could have been the reason for the large deviation in the results. We recalibrated the device to adjust the light source and got relatively better results, that were closer to the 550 nm peak of Au NP. We have now set up the platform inside the Plastic case in order to make measurements with liquid samples, in horizontal position. We have also started a fresh surface chemistry for using the portable LSPR

device in the horizontal position, for making measurements with liquid samples. The calibration of the device is depicted below:

Figure 48: Fiber Optic Cable for calibrating the intensity of the light beam

Each time we calibrate we measure the distance to the actual chip, so that there is reliability when we repeat the calibration for a different configuration. This experiment had 8.2 inches between light source and screen as shown below.

After calibrating the device, we did a verification step, by comparing experimental data with theoretical formulation of absorption. The below formula can be used to compute the expected absorption in a sample.

$$A_\lambda = -\log_{10}\left(\frac{S_\lambda - D_\lambda}{R_\lambda - D_\lambda}\right)$$

S_λ = Sample intensity at wavelength λ

D_λ = Dark intensity at wavelength λ

R_λ = Reference intensity at wavelength λ

$A_\lambda\ a.u.$	$A_{experimental}$
0.0048	0.005

Table A2: Validation of device calibration by using the absorption formula

In order to use the Portable LSPR device, we also need to select an appropriate substrate for the chips, that can be used for making the measurements [49]. The following brands with non-Gamma radiation sterilized plastics were tested for their absorption spectrum: Falcon, Costa, BD Falcon, Med supply. The results obtained are plotted below.

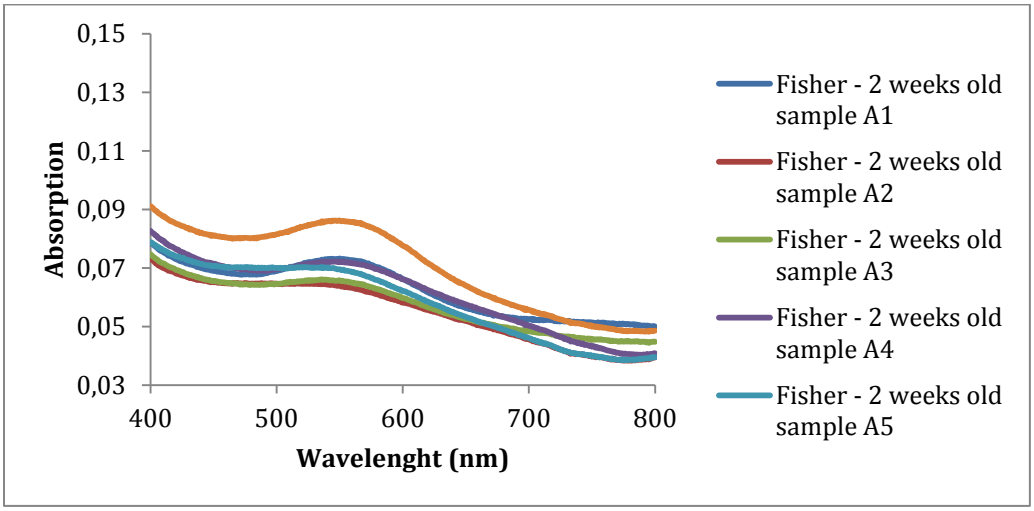

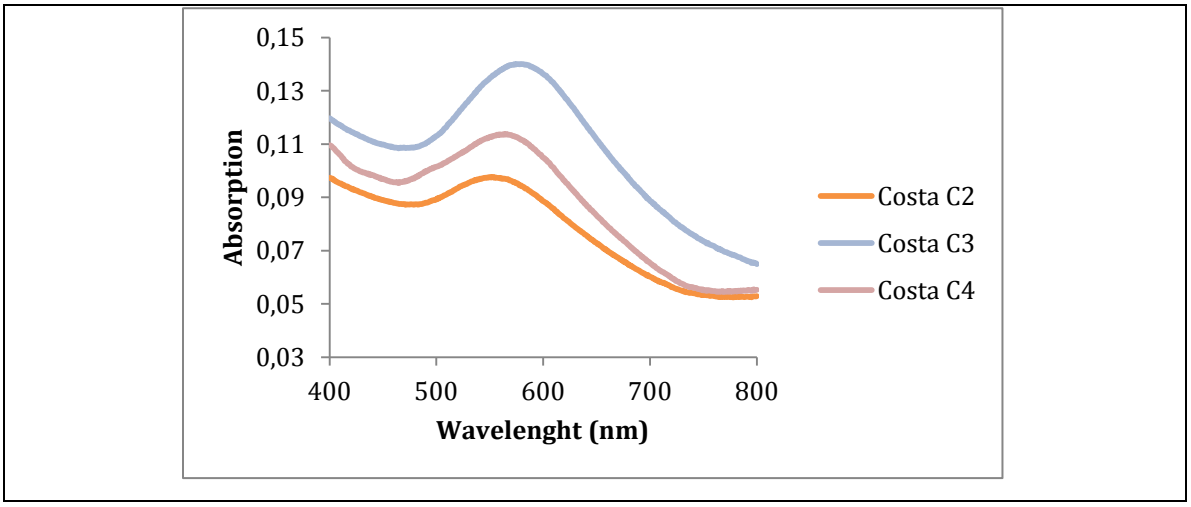

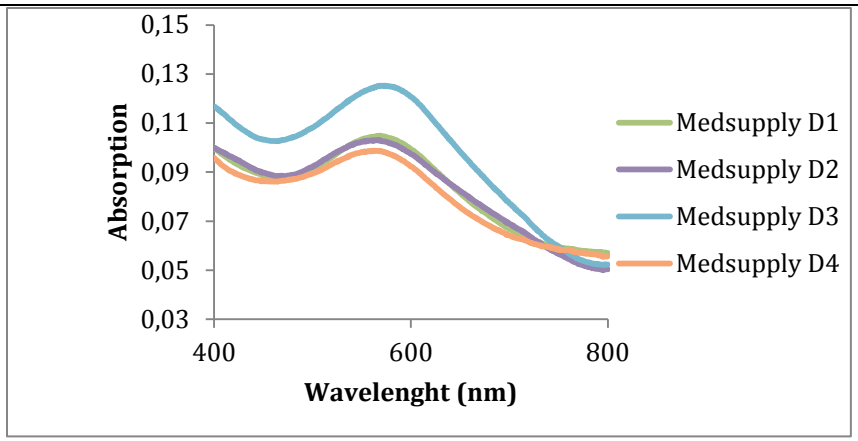

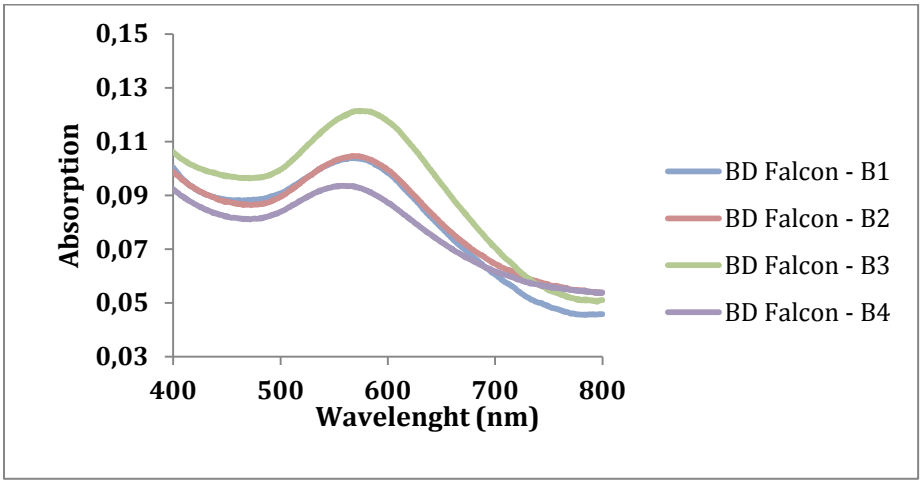

Figure 49 : Absorption spectra for each type of substrate.

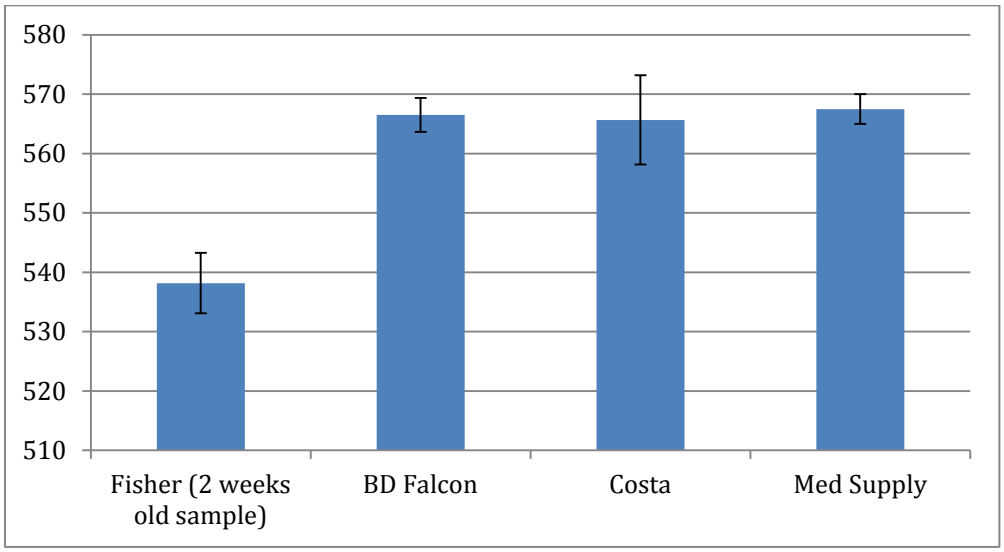

Plot obtained from Portable LSPR device with BD Falcon substrate and Au NP (MATLAB Plot) and a sample Plot from Ocean Optics Software of Portable LSPR are displayed below in Figure 42 and Figure 43. The MATLAB program using to find and plot the peak are shown in Appendix A.

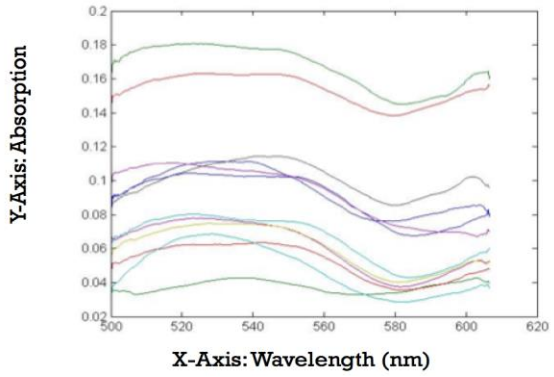

Figure 54: **Absorption plots after MATLAB smoothing**.

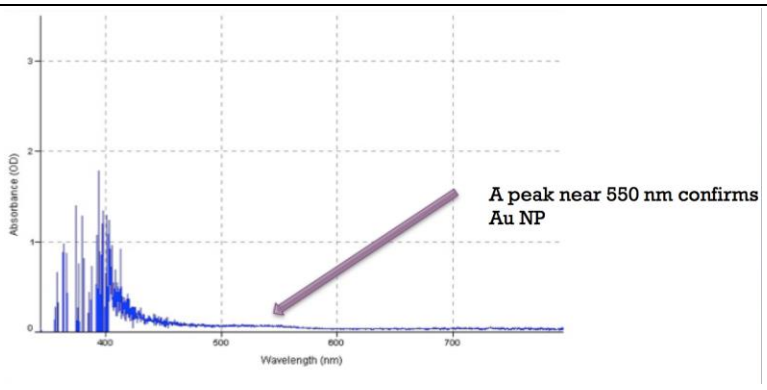

Figure 51: Ocean Optics plot pre-processing with MATLAB

The whole set-up was mounted inside the plastic container to tilt the chip-slot to horizontal position.

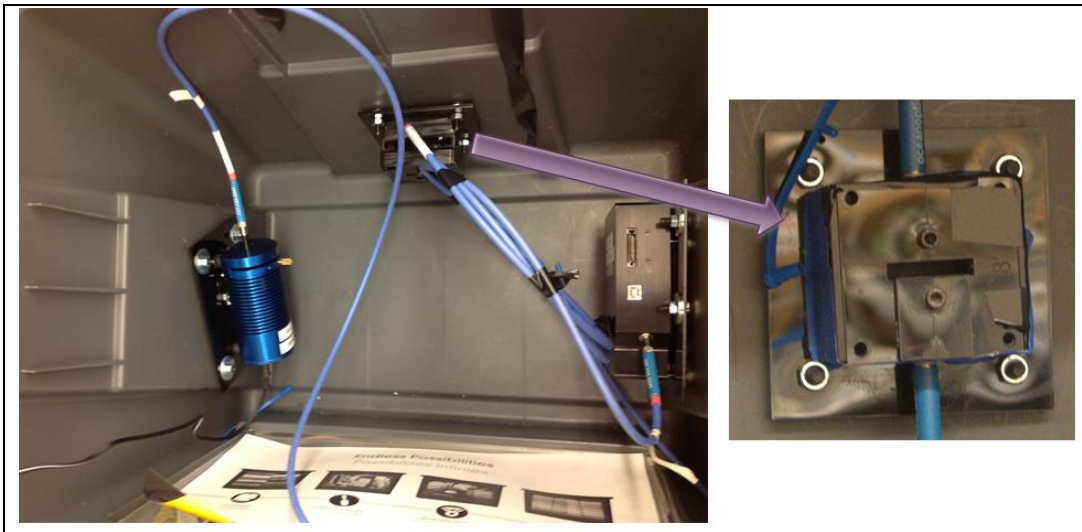

Figure 52: Internal view of the assembled portable LSPR

We have also changed the design of the chip, in order to obtain multiple data points per channel. The new design is also adjusted to the size of the collimated beam of light from the Source Lamp in the Portable LSPR device.

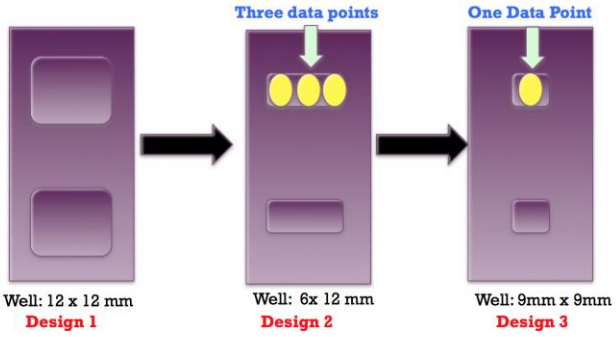

Figure 53: Old chip design for Portable LSPR and the new Chip design

The chip was constructed by fixing the glass slide to PMMA and DSA layer cut with a laser cutter machine.

We prepared chips for testing the Portable LSPR device. We have completed the following Surface Chemistry.

1. 150µL of 0.05mg/ml PLL in PBS → Incubation at 4° overnight
2. 150µL of AuNP → Incubation at 4° overnight
3. 150µL of 1mM MUA in PBS → Incubation at 4° for 3 hours.
4. 150µL of 191,7mg EDC+ 57,55mg NHS in MES Buffer (10ml) →Incubation at 4° overnight
5. 150µL of NeutrAvidin→ Incubation at 4° overnight

The working of the portable LSPR device is based on the absorption spectra measurements. When light is passed though the PMMA-BD Falcon substrate chips, a fraction of the light is absorbed and the remaining components are transmitted. The spectrum peaks at wavelengths that got absorbed. Beer Lamberts law states that:

$$A = \log (I_0/I)$$

where A is the absorbance, I is the intensity of transmitted light and I_0 the intensity of incident light. An alternate version to the law is

$$A= C*d* E$$

where C is the molar concentration, d is the path length and E is the molar absorption coefficient. However on using transparent PMMA chips, we observe that the data has too much of noise. The possible source for this noise is from scattering of light and diffraction at the chip edges. In order to test our hypothesis, we have designed the experiment with Black PMMA chips that can prevent light scattering and multiple internal diffraction effect.

The results we obtained can be summarized as below:

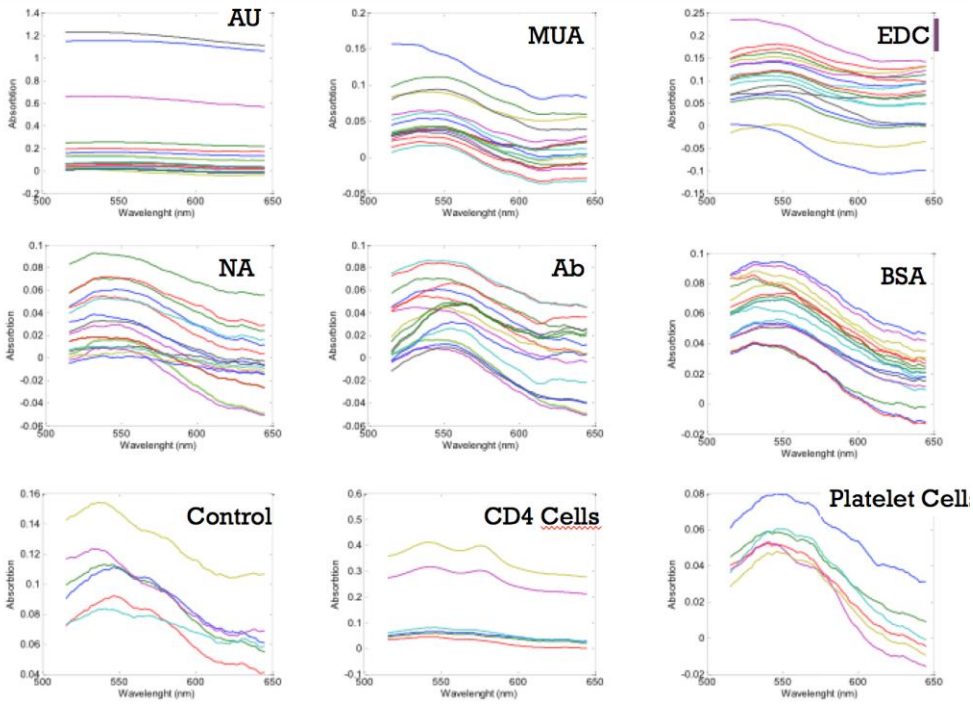

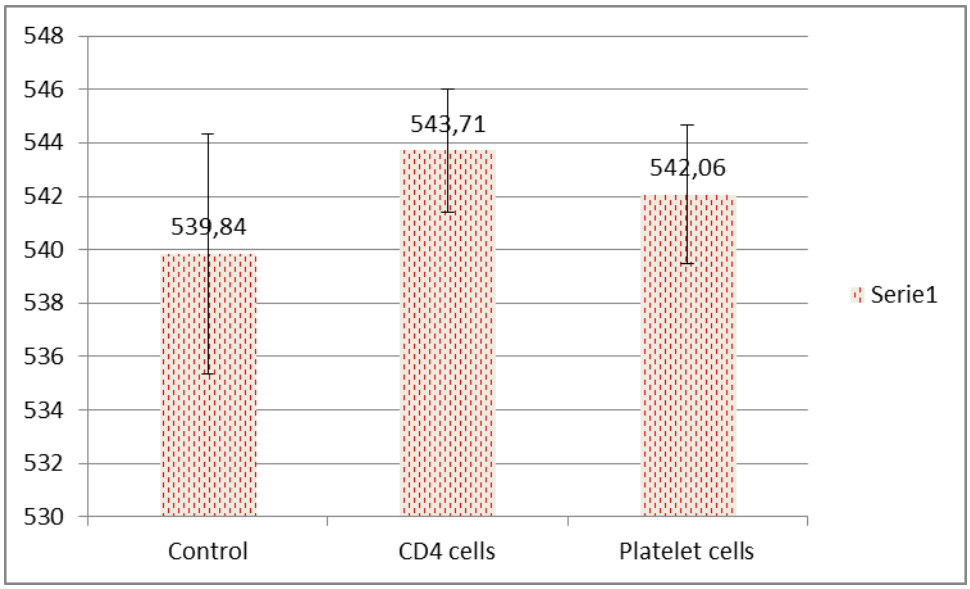

Figure 54: Comparison of different wavelength peaks (nm) of CD4 and Platelet cells

Conclusion

- Since there are small deviation from the expected trend in wavelength shift, we should repeat the surface chemistry to double check the data points, so that we can eliminate the possibility of human error while taking the measurement.

- There could be a possible mathematical relationship between the amount of captured cells and the amount of peak shift

- If we can determine this trend, then this platform can be multiplexed for detection many different types of pathogen based on the same principle

CONCLUSION

In this report we have discussed various developments in the field of MEMS and nanotechnology addressing global healthcare challenges like early stage detection of infectious diseases by bringing the needed primary intervention at the point-of-care, i.e. closer to the patient, in resource constrained settings. In Chapter 1 we have briefly reviewed the work done by U. Demirci and Ali K. et al. [1] that covers a broad areas in lab-on-chip based technologies that integrates with CCD, or mobile phones and optical microscopes for pathogen detection. In Chapter 2 we have examined the detailed physics involved in the principle of Localized Surface Plasmon Resonance, a technique that relies on the change in wavelength shift and extinction intensity coefficient for the detection of pathogen and characterization of different types of viruses. The important advantage of LSPR based microfluidic detection platform is the label free nature of detection., which is not achievable through conventional gold standard techniques like ELISA. In Chapter 3 we have seen how *E. coli* can be detected using lab-on-chip and have seen the associated surface chemistry that can be used to capture the bacteria from various sources like whole milk, phosphate buffer saline, human blood, or from spinach. Life threatening conditions like sepsis that arise due to *E. coli* infection has serious side effects like organ failure, increased blood lactose content, etc. are important factors for consideration to develop better and more affordable POC technologies that can be deployed in developing countries. In Chapter 4 we have presented an extensive report of the work done at the BAMM labs towards a nanoplasmonic platform that can detect viruses using a microfluidic platform. We demonstrate the ability to detect and quantify subtype A, B, C, D, E, G and panel of HIV with a specificity of under 100 copies/mL using both whole blood sample and HIV-patient blood sample discarded from clinics and this was compared against the gold standard using Reverse Transcriptase Polymerase Chain Reaction (RT-PCR). This microfluidic device has a total evaluation time for the assays of about 70 minutes, where 60 minutes is needed for capture and 10 minutes for data acquisition and processing. This LOC platform eliminates the need for any sample preparation before processing. This platform is highly multiplexable as the same surface chemistry can be adapted to capture and detect several other pathogens like dengue virus, *E. coli*, *M. tuberculosis*, etc. We also perform surface characterization using Atomic

Force Microscopy when the surface has polystyrene, Poly-L-Lysine, and Gold nanoparticle (AuNP). In the below diagram we illustrate the overall surface chemistry of the LSPR plates for detecting HIV subtypes. In chapter 6 we discuss the possibility to make the LSPR portable. We present the firsts steps toward this new challenge project that is still in progress.

In conclusion, the breadth of this report shows the promise in continuing research on point-of-care devices that can address one of the most pressing challenges in global healthcare of bringing the patient closer to the technology for disease detection and also to make such novel technologies affordable. Potential extension of the work presented here includes, early stage cancer detection by sensing cancer biomarkers, CTC's or other suitable indicators like siRNA.

ACKNOLEDGMENT

I am especially grateful to my research advisor Prof. Emanuele Domenico Giordano for his valuable help, supporting me all through the way until the completion of the project, and for his lovely patience with all my request. I'm thankful for his help, contributions and hidden support towards development of this project and above all in the most critical moment. His remarks and observations have helped me to improve the quality of my work.

It is a great pleasure to thank my second research advisor Dr Utkan Demirci for providing me this opportunity and having offered me the possibility to work on this exciting research project. I deeply value his brilliant advice and support which not only encouraged me in developing the project but also for my future career.

I would like to express all my gratitude to my supervisor Fatih Inci, for his dedication and guidance. I am thankful to him for enlightening me with his immense knowledge in the field and discussing the key point of the project I truly appreciated the amount of time and energy he invested to guided me throughout this work.

Finally I am very thankful to all the people who are involved in this project directly or indirectly. It was a great opportunity for me to work on this topic, and learn from my experiences. It has been a pleasure collaborating with all the members of the BAMM Labs and I sincerely appreciate their warm and cordial personalities. I spent in Boston the best experience in my life thanks to all of you.

REFERENCES

[1] Won G. L.; Kim, Y-G,; Chung, B. G.; Demirci, U.; Khademhosseini A., "Nano/Microfluidics for diagnosis of infectious diseases in developing countries", Elsevier Advanced Drug Delivery Review, 2009

[2] Anal Bioanal Chem (2004) 379: 920–930. DOI 10.1007/s00216-004-2708-9 , Amanda J. Haes Richard P, Van Duyne.

[3] IEEE Sensors Journal, Vol. 11, No. 2, February 2011, Andrii M. Lopatynskyi, Olga G. Lopatynska, L. Jay Guo, and Volodymyr I. Chegel, Science and Technology of Advanced Materials 8 (2007) 331–338 , "A localized surface plasmon resonance immunosensor for the detection of casein in milk"

[4] Sainsbury, T.; Ikuno, T.; Okawa, D.; Frechet, J.; Zettl, A., Self assembly of gold nanoparticle at the surface of amine- and Thiol- functionalized boron nitride nanotubes. J. Phys. Chem. C 2007, 111, 12991-12999

[5] Wang, S.; Esfahani, M.; Gurkan, U. A.; Inci, F.; Kuritzkes, D. R.; Demirci, U., Efficient On- Chip Isolation of HIV Subtypes. Lab Chip 2012, 12, 1508-1515.

[6] Manak, M.; Sina, S.; Anekella, B.; Hewlett, I.; Sanders-Buell, E.; Ragupathy, V.; Kim, J.; Vermeulen, M.; Stramer, S. L.; Sabino, E.; et al., Pilot Studies for Development of an HIV Subtype Panel for Surveillance of Global Diversity. AIDS Res. Hum. Retroviruses 2012, 28, 594-606.

[7] Decuzzi, P.; Ferrari, M., The Adhesive Strength of Non-spherical Particles Mediated by Specific Interactions. Biomaterials 2006, 27, 5307-5314.

[8] Shafiee, H., Jahangir, M., Inci, F., Wang, S., Willenbrecht, R.B., Giguel, F.F., Tsibris, A.M., Kuritzkes, D.R., and Demirci, U., *Acute On-Chip HIV Detection Through Label-Free Electrical Sensing of Viral Nano-Lysate.* Small, 2013.; doi:10.1002/smll.201202195

[9] Wang, S., Inci, F., De Libero, G., Singhal, A., and Demirci, U., *Point-of-care assays for tuberculosis: Role of nanotechnology/microfluidics.* Biotechnology Advances, 2013. **31**(4): p. 438-449., doi:10.1016/j.biotechadv.2013.01.006.

[10] Wang, S., Inci, F., Chaunzwa, T.L., Ramanujam, A., Vasudevan, A., Subramanian, S., Chi Fai Ip, A., Sridharan, B., Gurkan, U.A., and Demirci, U., Portable microfluidic chip for detection of Escherichia coli in produce and blood. Int J Nanomedicine, 2012. 7: p. 2591-600.; doi:10.2147/IJN.S29629

[11] Inci, F.*, Tokel, O.*, Wang, S., Gurkan, U.A., Tasoglu, S., Kuritzkes, D.R., and Demirci, U.,*Nanoplasmonic Quantitative Detection of Intact Viruses from Unprocessed Whole Blood.* ACS Nano, 2013., DOI: 10.1021/nn3036232.

[12] Demirci, U. (Author, Editor), Khademhosseini, A. (Editor), Langer, R. (Editor), and Blander, J. (Editor) "Microfluidic Technologies for Human Health". Publisher: World Scientific Publishing Company, ISBN-10: 9814405515, ISBN-13: 978-9814405515

[13] Berkley, S.; Bertram, K.; Delfraissy, J.-F.; Draghia-Akli, R.;Fauci, A.; Hallenbeck, C.; Kagame, M. J.; Kim, P.; Mafubelu, D.; Makgoba, M. W.; et al. The 2010 Scientific Strategic Plan of the Global HIV Vaccine Enterprise. Nat. Med. 2010, 16, 981–989.

[14] World Health Organization, Global Health Observatory(GHO) - HIV/AIDS. 2012, Available at: www.who.int/gho/hiv/en/index.html. Accessed May 4, 2013.

[15] Karst, S. M. Pathogenesis of Noroviruses, Emerging RNA Viruses. Viruses 2010, 2, 748–781.

[16] Kulinski, M. D.; Mahalanabis, M.; Gillers, S.; Zhang, J. Y.; Singh, S.; Klapperich, C. M. Sample Preparation Module for Bacterial Lysis and isolation of Human DNA form urine", Biomed Microdevices. 2009 Jun;11(3):671-8. doi: 10.1007/s10544-008-9277-1.

[17] Katherine A.Willets and Richard P. Van Duyne, "Localized Surface Plasmon Resonance Spectroscopy and Sensing", DOI: 1146/annurev.physchem. 58.032806.104607

[18] Madigan M, Martinko J (editors). (2005). Brock Biology of Microorganisms (11th ed. ed.). Prentice Hall. ISBN 0-13-144329-1.

[19] R. V. Lapshin (2011). "Feature-oriented scanning probe microscopy" In H. S. Nalwa. ,American Scientific Publishers. pp. 105–115. ISBN 1-58883-163-9.

[20] Patolsky, F.; Zheng, G.; Lieber, C. M. Nanowire Sensors for Medicine and the Life Sciences. Nanomedicine (London, U. K.) 2006, 1, 51–65.

[21] Barone, P. W.; Strano, M. S. Single Walled Carbon Nanotubes as Reporters for The Optical Detection of Glucose. J. Diabetes Sci. Technol. 2009, 3, 242–252.

[22] Williams, E. H.; Schreifels, J. A.; Rao, M. V.; Davydov, A. V.; Oleshko, V. P.; Lin, N. J.; Steffens, K. L.; Krylyuk, S.; Bertness, K. A.; Manocchi, A. K.; et al. Selective Streptavidin Bioconjugation on Silicon and Silicon Carbide Nanowires for Biosensor Applications. J. Mater. Res. 2012, 1–10.

[23] Zhang, G.-J.; Zhang, L.; Huang, M. J.; Luo, Z. H. H.; Tay, G. K. I.; Lim, E.-J. A.; Kang, T. G.; Chen, Y. Silicon Nanowire Biosensor for Highly Sensitive and Rapid Detection of Dengue Virus. Sens. Actuators, B 2010, 146, 138–144.

[24] Kuzmych, O.; Allen, B. L.; Star, A. Carbon Nanotube Sensors for Exhaled Breath Components. Nanotechnology 2007, 18.

[25] Kim, Y.-G.; Moon, S.; Kuritzkes, D. R.; Demirci, U. Quantum Dot-Based HIV Capture and Imaging in a Microfluidic Channel. Biosens. Bioelectron. 2009, 25, 253–258.

[26] Gurkan, U. A.; Moon, S.; Geckil, H.; Xu, F.; Wang, S.; Lu, T. J.; Demirci, U. Miniaturized Lensless Imaging Systems for Cell and Microorganism Visualization in Point-of-Care Testing. Biotechnol. J. 2011, 6, 138–149.

[27] Jung LS, Campbell CT. Sticking probabilities in adsorption from liquid solutions: alkylthiols on gold. Phys. Rev. Lett. 84(22), 5164–5167 (2000).

[28] Perez-Luna VH, O'Brien MJ, Opperman KA et al. Molecular recognition between genetically engineered streptavidin and surface-bound biotin. J. Am. Chem. Soc. 121(27), 6469–6478 (1999).

[29] Georgiadis R, Peterlinz KP, Peterson AW. Quantitative measurements and modeling of kinetics in nucleic acid monolayer films using SPR spectroscopy. J. Am. Chem. Soc. 122(13), 7837–3173 (2000).

[30] Hall D. Use of optical biosensors for the study of mechanistically concerted surface adsorption processes. Anal. Biochem. 288(2), 109–125 (2001).

[31] Haake H-M, Schutz A, Gauglitz G. Label-free detection of biomolecular interaction by optical sensors. Fresenius' J. Anal. Chem. 366(6–7), 576–585 (2000).

[32] Shumaker-Parry JS, Zareie MH, Aebersold R, Campbell CT. Microspotting streptavidin and double-stranded DNA arrays on gold for high-throughput studies of protein–DNA interactions by surface plasmon resonance microscopy. Anal. Chem. 76(4), 918–929 (2004).

[33] Malinsky MD, Kelly KL, Schatz GC, Van Duyne RP. Chain length dependence and sensing capabilities of the localized surface plasmon resonance of silver nanoparticles chemically modified with alkanethiol self-assembled monolayers. J. Am. Chem. Soc. 123(7), 1471–1482 (2001).

[34] Haes AJ, Van Duyne RP. A nanoscale optical biosensor: sensitivity and selectivity of an approach based on the localized surface plasmon resonance spectroscopy of triangular silver nanoparticles. J. Am. Chem. Soc. 124(35), 10596–10604 (2002).

[35] Riboh JC, Haes AJ, McFarland AD, Yonzon CR, Van Duyne RP. A nanoscale optical biosensor: real-time immunoassay in physiological buffer enabled by improved nanoparticle adhesion. J. Phys. Chem. B107, 1772–1780 (2003).

[36] McFarland AD, Van Duyne RP. Single silver nanoparticles as real-time optical sensors with zeptomole sensitivity. Nano. Lett. 3, 1057–1062 (2003).

[37] Zeng, S.; Yong, Ken-Tye; Roy, Indrajit; Dinh, Xuan-Quyen; Yu, Xia; Luan, Feng (2011). "A review on functionalized gold nanoparticles for biosensing applications". Plasmonics 6 (3): 491–50

[38] Liedberg, Bo; Nylander, Claes; Lunström, Ingemar (1983). "Surface plasmon resonance for gas detection and biosensing". Sensors and Actuators 4: 299

[39] Minh Hiep, Ha; Endo, Tatsuro; Kerman, Kagan; Chikae, Miyuki; Kim, Do-Kyun; Yamamura, Shohei; Takamura, Yuzuru; Tamiya, Eiichi (2007). "A

localized surface plasmon resonance based immunosensor for the detection of casein in milk". Sci. Technol. Adv.

[40] Hikmat N. Daghestani and Billy W. Day. “Theory and Applications of Surface Plasmon Resonance, Resonant Mirror, Resonant Waveguide Grating, and Dual Polarization Interferometry Biosensors” Sensor Review

[41] Homola J.,Surface Plasmon Resonance for Detection of Chemical and Biological Species, Chemical Reviews, American Chemical Society, 2008, Vol 108, No. 2.

[42] Nikmat N. Daghestani and W. Day, Theory and Applications of Surface Plasmon Resonance, Resonant Mirror, Resonant Waveguide Grating, and Dual Polarization Interferometry Biosensors, Review, Sensors, 2010.

[43] Konstantinos A (2010). "Testing for tuberculosis". Australian Prescriber 33 (1): 12–18.

[44] World Health Organization (2009). "Epidemiology". Global tuberculosis control: epidemiology, strategy, financing. pp. 6–33

[45] Lawn SD, Bangani N, Vogt M, et al. (2007). "Utility of interferon-γ ELISPOT assay responses in highly tuberculosis-exposed patients with advanced HIV infection in South Africa". BMC Infectious Diseases

[46] Antman, K.; Chang, Y. (2000). "Kaposi's Sarcoma". New England Journal of Medicine 342 (14): 1027–1038

[47] Schwartz, R.; Micali, G.; Nasca, M.; Scuderi, L. (2008). "Kaposi sarcoma: A continuing conundrum". Journal of the American Academy of Dermatology 59 (2): 179–206; quiz 207–8

[48] "Epilepsy". Fact Sheets. World Health Organization. October 2012. Retrieved January 24, 2013.
[49] HR2000 and HR2000CG-UV-NIR Series High-Resolution Fiber Optic Spectrometers. HR2000 / HR2000CG-UV-NIR. Installation and Operation Manual

APPENDIX A

Matlab program to find the wavelength peak.

```
clear all;
close all;
clc;
filenamesuffix = '.txt';
TotalNumberofSamples = 16;
DataForEachSample = 3;
Datasuffixforsamples = ['a' 'b' 'c'];
LowPassParameter = 100;
ConsideredPartStart =475;
ConsideredPartEnd = 650;



filenameDirectory = '122113LSPRAfterGold\';

CalculationForPeakFinder

DataAfterGold = [FreqAxis TempDataSet];
SmoothedDataAfterGold = [FreqAxis SmoothedTempData];
WavelenghtMaxPeakIndexAfterGold=WavelenghtMaxPeakIndex;
DataAfterGoldPart = [FreqAxisPart TempDataSetPart(RLPP:end-RLPP,:)];
SmoothedDataAfterGoldPart = [FreqAxisPart SmoothedTempDataPart];
WavelenghtMaxPeakIndexPartAfterGold=WavelenghtMaxPeakIndexPart;

filenameDirectory = '122113LSPRafterMUA\';

CalculationForPeakFinder


DataAfterMUA = [FreqAxis TempDataSet];
SmoothedDataAfterMUA = [FreqAxis SmoothedTempData];
WavelenghtMaxPeakIndexAfterMUA=WavelenghtMaxPeakIndex;
DataAfterMUAPart = [FreqAxisPart TempDataSetPart(RLPP:end-RLPP,:)];
SmoothedDataAfterMUAPart = [FreqAxisPart SmoothedTempDataPart];
WavelenghtMaxPeakIndexPartAfterMUA=WavelenghtMaxPeakIndexPart;



filenameDirectory = '122113LSPRafterEDCNHS\';

CalculationForPeakFinder


DataAfterEDCNHS = [FreqAxis TempDataSet];
SmoothedDataAfterEDCNHS = [FreqAxis SmoothedTempData];
WavelenghtMaxPeakIndexAfterEDCNHS=WavelenghtMaxPeakIndex;
DataAfterEDCNHSPart = [FreqAxisPart TempDataSetPart(RLPP:end-RLPP,:)];
SmoothedDataAfterEDCNHSPart = [FreqAxisPart SmoothedTempDataPart];
WavelenghtMaxPeakIndexPartAfterEDCNHS=WavelenghtMaxPeakIndexPart;
```

```
filenameDirectory = '122113LSPRafterNA\';

CalculationForPeakFinder


DataAfterNA = [FreqAxis TempDataSet];
SmoothedDataAfterNA = [FreqAxis SmoothedTempData];
WavelenghtMaxPeakIndexAfterNA=WavelenghtMaxPeakIndex;
DataAfterNASPart = [FreqAxisPart TempDataSetPart(RLPP:end-RLPP,:)];
SmoothedDataAfterNAPart = [FreqAxisPart SmoothedTempDataPart];
WavelenghtMaxPeakIndexPartAfterNA=WavelenghtMaxPeakIndexPart;


ShiftValues=[WavelenghtMaxPeakIndexAfterGold
WavelenghtMaxPeakIndexAfterMUA WavelenghtMaxPeakIndexAfterNA...
    WavelenghtMaxPeakIndexPartAfterGold
WavelenghtMaxPeakIndexPartAfterMUA WavelenghtMaxPeakIndexPartAfterNA]
ShiftAmount=[WavelenghtMaxPeakIndexAfterGold-
WavelenghtMaxPeakIndexAfterMUA ...
    WavelenghtMaxPeakIndexPartAfterGold-
WavelenghtMaxPeakIndexPartAfterMUA ...
    WavelenghtMaxPeakIndexPartAfterGold-
WavelenghtMaxPeakIndexPartAfterNA]

MeanShiftValuesGraph=mean([ShiftValues(7:end,4) ShiftValues(7:end,5)
ShiftValues(7:end,6)])
StdShiftValuesGraph=std([ShiftValues(7:end,4) ShiftValues(7:end,5)
ShiftValues(7:end,6)])

MeanShiftAmountGraph=mean(ShiftAmount(7:end,2))
StdShiftAmountGraph=std(ShiftAmount(7:end,2))

MeanShiftValuesGraph=mean([ShiftValues(7:end,3) ShiftValues(7:end,4)])
StdShiftValuesGraph=std([ShiftValues(7:end,3) ShiftValues(7:end,4)])

MeanShiftAmountGraph=mean(ShiftAmount(7:end,2))
StdShiftAmountGraph=std(ShiftAmount(7:end,2))

figure;
bar(MeanShiftValuesGraph,0.1);
hold on
errorbar(MeanShiftValuesGraph,StdShiftValuesGraph,'r.')
grid minor
xlabel('Wavelength measurements after given step');
ylabel('Wavelength');
set(gca,'XTickLabel',{ 'Gold','MUA'});

ShiftValues=[WavelenghtMaxPeakIndexPartAfterGold...
    WavelenghtMaxPeakIndexPartAfterMUA...
    WavelenghtMaxPeakIndexPartAfterEDCNHS...
    WavelenghtMaxPeakIndexPartAfterNA]
ShiftAmount=[WavelenghtMaxPeakIndexPartAfterGold-
WavelenghtMaxPeakIndexPartAfterMUA ...
    WavelenghtMaxPeakIndexPartAfterMUA-
WavelenghtMaxPeakIndexPartAfterEDCNHS ...
    WavelenghtMaxPeakIndexPartAfterEDCNHS-
WavelenghtMaxPeakIndexPartAfterNA]
```

```
MeanShiftValuesGraph=mean(ShiftValues(7:end,:))
StdShiftValuesGraph=std(ShiftValues(7:end,:))

MeanShiftAmountGraph=mean(ShiftAmount(7:end,:))
StdShiftAmountGraph=std(ShiftAmount(7:end,:))

figure;
bar(MeanShiftValuesGraph,0.1);
hold on
errorbar(MeanShiftValuesGraph,StdShiftValuesGraph,'r.')
grid minor
xlabel('Wavelength measurements after given step');
ylabel('Wavelength');
set(gca,'XTickLabel',{ 'Gold','MUA', 'EDC NHS', 'NA'});

ShiftValues=[WavelenghtMaxPeakIndexPartAfterGold...
    WavelenghtMaxPeakIndexPartAfterMUA...
    WavelenghtMaxPeakIndexPartAfterEDCNHS...
    WavelenghtMaxPeakIndexPartAfterNA]
ShiftAmount=[WavelenghtMaxPeakIndexPartAfterGold-
WavelenghtMaxPeakIndexPartAfterMUA ...
    WavelenghtMaxPeakIndexPartAfterMUA-
WavelenghtMaxPeakIndexPartAfterEDCNHS ...
    WavelenghtMaxPeakIndexPartAfterEDCNHS-
WavelenghtMaxPeakIndexPartAfterNA]

MeanShiftValuesGraph=mean(ShiftValues(7:end,:))
StdShiftValuesGraph=std(ShiftValues(7:end,:))

MeanShiftAmountGraph=mean(ShiftAmount(7:end,:))
StdShiftAmountGraph=std(ShiftAmount(7:end,:))

figure;
bar(MeanShiftValuesGraph,0.1);
hold on
errorbar(MeanShiftValuesGraph,StdShiftValuesGraph,'r.')
grid minor
xlabel('Wavelength measurements after given step');
ylabel('Wavelength');
set(gca,'XTickLabel',{ 'Gold','MUA', 'EDC NHS', 'NA'});


% close all;
%
% for i=1:TotalNumberofSamples
%         figure;
%         plot(FreqAxisPart, SmoothedDataAfterNAPart(:,(i-
1)*DataForEachSample+1));
%         hold on
%         plot(FreqAxisPart, SmoothedDataAfterNAPart(:,(i-
1)*DataForEachSample+2),'r');
%         plot(FreqAxisPart, SmoothedDataAfterNAPart(:,(i-
1)*DataForEachSample+3),'g');
%         hold off
%
% end
```

```
%
% DataAfterNA = [FreqAxis TempDataSet];
% SmoothedDataAfterNA = [FreqAxis SmoothedTempData];
% WavelenghtMaxPeakIndexAfterNA=WavelenghtMaxPeakIndex;
% DataAfterNASPart = [FreqAxisPart TempDataSetPart(RLPP:end-RLPP,:)];
% SmoothedDataAfterNAPart = [FreqAxisPart SmoothedTempDataPart];
% WavelenghtMaxPeakIndexPartAfterNA=WavelenghtMaxPeakIndexPart;
```

APPENDIX A

Artificial Saliva Recipe (can be stored for 1-2 weeks)

Reference: "Galvanic currents between dental alloys in vitro" K ARVIDSON **et al. (1985)**

Artificial saliva has the following composition: 0.1 L each of 25 mM K2PO4, 24 Mm Na2HPO4,150 mM KHCO3, 1.5 Mm MgCl2. 0.006 L of 25 mM citric acid, and 0.1 L of 15 mM CaCl2 will be added to this solution.

Salt	**MW (g/mol)**	**Molarity (mM=mmol/L)**	**Volume (L)**	**Weight (mg)**
K2HPO4	174.2	25	0.1	435.5
Na2HPO4	141.96	24	0.1	340.704
KHCO3	100.115	150	0.1	1501.725
NaCl	58.443	100	0.1	584.43
MgCl2	203.31	1.5	0.1	30.4965
Citric acid	192.124	25	0.006	28.8186
CaCl2	147.014	5	0.1	73.507

To achieve a pH of 6.7 either add NaOH or HCl to the solution and adjust volume to 1L.

- Proteins can be added to this solution.
  40 mg/L Albumin (Bovine serum albumin) and 850 mg/ml mucin (bovine submaxillary mucin)

Reference for proteins:

1. Rheological aspects of mucin-containing solutions and saliva substitutes (1992)
2. Influence of saliva substitute films on Streptoccous mutans (2008)